

Cosmic-Ray Feedback from Supernovae in a Stratified Interstellar Medium

ROARK HABEGGER ¹ AND ELLEN G. ZWEIBEL ^{1,2}

¹*University of Wisconsin-Madison Astronomy Department*

²*University of Wisconsin-Madison Physics Department*

ABSTRACT

Each supernova’s energy drives interstellar medium (ISM) turbulence and can help launch galactic winds. What difference does it make if 10% of the energy is initially deposited into cosmic rays? To answer this question and study cosmic-ray feedback, we perform galactic patch simulations of a stratified ISM. We compare two magnetohydrodynamic and cosmic ray (MHD+CR) simulations, which are identical except for how each supernova’s energy is injected. In one, 10% of the energy is injected as cosmic-ray energy and the rest is thermal. In the other case, energy injection is strictly thermal. We find that cosmic-ray injections (1) drive a faster vertical motion with more mass, (2) produce a more vertically oriented magnetic field, and (3) increase the scale height of warm gas outside the midplane ($z \gtrsim 0.5$ kpc). Both simulations show the formation of cold clouds (with a total mass fraction $> 50\%$) through the Parker instability and thermal instability. We also show that the Parker instability leads to a decorrelation of cosmic-ray pressure and gas density. Finally, our simulations show that a vertical magnetic field can lead to a significant decrease in the calorimetric fraction for injected cosmic rays.

Keywords: Cosmic Rays (329) - Magnetohydrodynamical simulations (1966) - Galaxy Structure (622)

1. INTRODUCTION

A tenth, 10%, or 0.1 of anything is a small fraction. Neglecting such a small component is a reasonable assumption in many situations. An example of this small component is cosmic rays in the interstellar medium (ISM): 10% of each supernova’s kinetic energy is all that is needed to explain the amount of these high-energy particles in our galaxy’s ISM (Baade & Zwicky 1934; Blandford & Ostriker 1978). More recent work has illustrated that the fraction produced in a shock could be as high as 20% (Caprioli & Spitkovsky 2014). That fraction could still be considered negligible, especially on the long time scales ($t \gtrsim 100$ Myr) and long length scales ($L \gtrsim 1$ kpc) of galaxy evolution, since supernovae drive turbulence and heat gas at small scales ($L \sim 1$ pc).

However, other work has shown that cosmic rays are not negligible on large scales (see recent reviews Zweibel (2017); Ruszkowski & Pfrommer (2023); Owen et al. (2023)). They are in approximate pressure/energy

equipartition with the thermal gas and magnetic field (Ferrière 2001). Gradients in cosmic-ray pressure can drive outflows or fountain flows from a galactic disk, removing gas that could otherwise form stars (Chan et al. 2022; Tsung et al. 2023; Armillotta et al. 2024; Thomas et al. 2024). Bottlenecks created by cosmic-ray streaming can destroy and disrupt cold gas clouds (Wiener et al. 2019; Bustard & Zweibel 2021; Tsung et al. 2022). Cosmic-ray transport is faster parallel to the magnetic field, and this anisotropic transport can impact the turbulent energy cascade of the thermal gas (Habegger et al. 2024).

These feedback mechanisms are stifled if cosmic rays are transported out of the galaxy too quickly. In order to keep global galaxy simulations (cosmological zoom-in simulations) in agreement with observed γ -ray luminosities, a cosmic-ray diffusion coefficient of about one order of magnitude higher than the standard value of $3 \times 10^{28} \text{ cm}^2 \text{ s}^{-1}$ derived from the B/C ratio (Jones et al. 2001; Evoli et al. 2020) is often invoked, following the simulations of Chan et al. (2019). This diffusion coefficient amplification means that the cosmic rays escape the galaxy before they ever affect the dynamics of the thermal gas. This result brings us back to the idea that

cosmic rays produce only a marginal effect; including them just makes stellar feedback slightly more efficient.

In this work, we examine how individual cosmic-ray sources eventually adjust the dynamics and vertical structure of the multiphase ISM, becoming a significant component of stellar feedback. We previously examined how a single localized cosmic-ray energy injection on a magnetic flux tube could disrupt a stratified ISM (Habegger et al. 2023). This work builds on that study to consider many injections throughout the galactic midplane. Our simulations evolve a slab of stratified ISM, with midplane parameters that match the solar neighborhood. After a significant fountain flow develops in the first 200 Myr, with magnetic field geometry similar to the Parker instability (Parker 1966), the slab reaches a steady state (lasting $\gtrsim 100$ Myr). During the transition to the steady state, the cosmic rays are able to escape quickly without interacting with the thermal gas. In the steady state, we show how individual cosmic-ray injections allow cosmic-ray pressure to be the primary force outside the galactic midplane.

Figure 1 is a snapshot of one of our simulations, which illustrates the complex temperature and magnetic field structures that form over time in the stratified, multiphase, and magnetized ISM. The temperature varies over several orders of magnitude. Individual magnetic field lines stretch over 1 kpc in length. Considering the full scale of a galaxy, those magnetic field lines would connect the galactic plane and the galactic halo. We find that these field lines act as escape highways for injected cosmic rays, keeping the simulation below the calorimetric limit. These extended field lines result from expanding plumes that push the horizontal magnetic field out of the galactic plane. Those plumes drive the creation of cold gas in valleys, the same structure predicted for the Parker instability (Parker 1966). **These valleys result in a decorrelation of cosmic-ray pressure and gas density.** The decorrelation is visible in Figure 1, where the cold gas (blue contours) and high cosmic-ray pressure regions (brown contours) alternate in the y direction, which is perpendicular to the mean magnetic field.

In Section 2, we detail our simulation setup, numerical methods, and implementation of physical processes. In Section 3, we cover the primary results from our simulations. In Section 4, we discuss several implications derived from our results and analysis. Finally, in Section 5, we provide a short summary and list of key conclusions.

2. METHODS

We use the astrophysical magnetohydrodynamic (MHD) simulation code *Athena++* to evolve a thermal

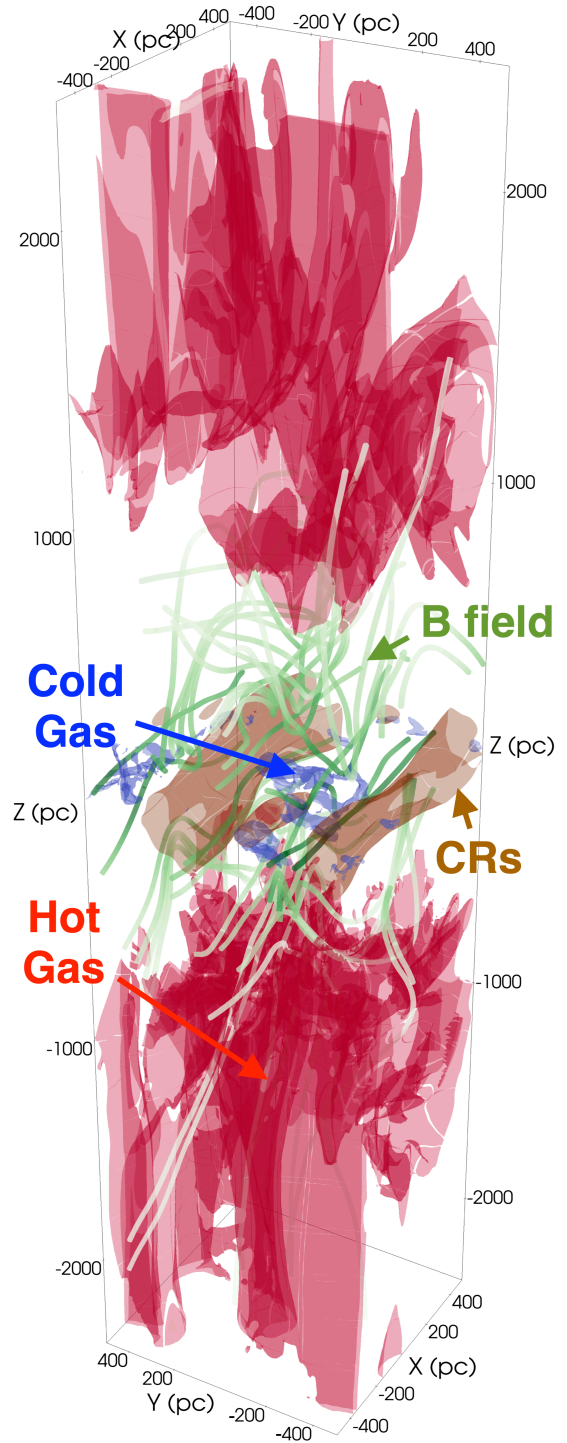


Figure 1. 3D snapshot at $t = 180$ Myr from our CRInj simulation (see Table 1). Small blue structures near $z = 0$ are contours around cold gas ($T \leq 500$ K), and the large red sheets at $|z| > 1000$ pc are contours around hot gas ($T \geq 2 \times 10^4$ K). Green lines trace the magnetic field, and darker green corresponds to stronger magnetic field. The brown contours in the $z = 0$ plane surround regions of high cosmic-ray pressure.

fluid alongside a cosmic-ray fluid (Stone et al. 2020; Jiang & Oh 2018). The code solves the following system of equations:

$$\frac{\partial \rho}{\partial t} + \nabla \cdot (\rho \mathbf{u}) = 0 \quad (1)$$

$$\frac{\partial \mathbf{B}}{\partial t} - \nabla \times (\mathbf{u} \times \mathbf{B}) = 0 \quad (2)$$

$$\frac{\partial \rho \mathbf{u}}{\partial t} + \nabla \cdot \left(\rho \mathbf{u} \mathbf{u} + \mathbb{1} \left(P_g + \frac{B^2}{2} \right) - \mathbf{B} \mathbf{B} \right) = \rho \mathbf{g} + \sigma_c \cdot \left(\mathbf{F}_c - \frac{4}{3} E_c \mathbf{u} \right) \quad (3)$$

$$\frac{\partial E}{\partial t} + \nabla \cdot \left(\left(E + P_g + \frac{B^2}{2} \right) \mathbf{u} - (\mathbf{B} \cdot \mathbf{u}) \mathbf{B} \right) = \rho \mathbf{g} \cdot \mathbf{u} + \mathcal{L}(n, T) - \frac{1}{3} (\mathbf{u} + \mathbf{v}_s) \cdot \nabla E_c \quad (4)$$

$$\frac{\partial E_c}{\partial t} + \nabla \cdot \mathbf{F}_c = \frac{1}{3} (\mathbf{u} + \mathbf{v}_s) \cdot \nabla E_c \quad (5)$$

$$\frac{1}{V_m^2} \frac{\partial \mathbf{F}_c}{\partial t} + \frac{1}{3} \nabla E_c = -\sigma_c \cdot \left(\mathbf{F}_c - \frac{4}{3} E_c \mathbf{u} \right). \quad (6)$$

These equations describe the evolution of a magnetized two-fluid system. The first fluid, thermal gas, has a mass density ρ , velocity \mathbf{u} , pressure P_g . The second fluid, made up of cosmic rays (i.e. a relativistic, non-thermal fluid), is described by a total energy density E_c and flux \mathbf{F}_c . The cosmic-ray transport coefficient σ_c is a diagonal matrix which governs how cosmic-ray energy moves in the simulation, \mathbf{v}_s is the streaming velocity, and the modified speed of light V_m sets the maximum transport speed. We evolve the magnetic field \mathbf{B} from Faraday's Law in the ideal MHD approximation (Eqn. 2). The remaining variables are the total magnetohydrodynamic energy density of the first fluid $E = P_g/(\gamma-1) + \rho u^2/2 + B^2/2$, the gravitational field \mathbf{g} , and the radiative heating and cooling function $\mathcal{L}(n, T)$, which depends on the number density ($n = \rho/m$, where m is particle mass) and temperature ($T = P_g m/(\rho k_B)$) of the thermal gas.

For the cosmic-ray transport, we allow the cosmic rays to diffuse along the local magnetic field at the canonical Milky Way value of $\kappa_{\parallel} = 3 \times 10^{28} \text{ cm}^2 \text{ s}^{-1}$ (Jones et al. (2001), for more recent observations see Evoli et al. (2019, 2020)). This anisotropic transport is created by splitting the transport coefficient into components perpendicular and parallel to the local magnetic field direction \hat{b} in each cell (see Jiang & Oh (2018)):

$$\sigma_{c,\text{diff}} = \frac{1}{\kappa_{\perp}} \mathbb{1} + \left(\frac{1}{\kappa_{\parallel}} - \frac{1}{\kappa_{\perp}} \right) \hat{b} \hat{b}. \quad (7)$$

For the perpendicular direction, we set the transport rate at $\kappa_{\perp} = 3 \times 10^{18} \text{ cm}^2 \text{ s}^{-1}$ so there is no diffusion perpendicular to the field over the course of the simulation (Desiati & Zweibel 2014). See Habegger et al. (2024) for an extended discussion on choosing the cosmic-ray diffusion coefficient in this anisotropic, resolved magnetic field treatment.

We also include the effects of cosmic-ray streaming transport. The additional heating from dissipation of Alfvén waves is included in the energy equations (MHD energy in Equation 4, cosmic-ray energy in Equation 5). The additional transport appears in the transport matrix by including the following term:

$$\sigma_{c,\text{str}} = -\hat{b} \hat{b} \frac{(\gamma_c - 1) \hat{b} \cdot \nabla E_c}{\gamma_c E_c \mathbf{v}_s \cdot \hat{b}} = -\hat{b} \hat{b} \frac{\hat{b} \cdot \nabla E_c}{4 E_c \mathbf{v}_s \cdot \hat{b}}. \quad (8)$$

Additionally, it is important to note that the streaming velocity should be

$$\mathbf{v}_s = -\frac{\mathbf{B} \cdot \nabla P_c}{\sqrt{4\pi\rho} |\mathbf{B} \cdot \nabla P_c|} \quad (9)$$

for the equations in Jiang & Oh (2018) to match with other formulations of the cosmic-ray energy equation (e.g. McKenzie & Voelk (1982); Breitschwerdt et al. (1991); Zweibel (2017)).

The total transport parallel to the magnetic field is the addition of the reciprocals of the transfer terms:

$$\frac{1}{\hat{b} \cdot \sigma_c \cdot \hat{b}} = \frac{1}{\hat{b} \cdot \sigma_{c,\text{diff}} \cdot \hat{b}} + \frac{1}{\hat{b} \cdot \sigma_{c,\text{str}} \cdot \hat{b}} = \kappa_{\parallel} - \frac{4 E_c \mathbf{v}_s \cdot \hat{b}}{\hat{b} \cdot \nabla E_c}. \quad (10)$$

This combination gives a final, total transport matrix of

$$\sigma_c = \frac{1}{\kappa_{\perp}} \mathbb{1} + \left(\frac{1}{\kappa_{\parallel} - \frac{4 E_c \mathbf{v}_s \cdot \hat{b}}{\hat{b} \cdot \nabla E_c}} - \frac{1}{\kappa_{\perp}} \right) \hat{b} \hat{b}. \quad (11)$$

This streaming and diffusion implementation is standard, and follows directly from Jiang & Oh (2018). We include it here in an effort to make Equations 5 & 6 clear to readers unfamiliar with Jiang & Oh (2018).

In the simulations used for this work, we used $V_m = 0.1c$. See Appendix C of Habegger et al. (2023) for an extended V_m convergence study. Our largest flow velocities are on the order of 100 km s^{-1} , much lower than our chosen V_m .

2.1. Setup & Initial Conditions

We present two simulations, with identical initial conditions, physics, and random seed. The only difference

Parameter	CRInj	NoCRInj
T_0/K		10^4
$\rho_0/(m_p \text{ cm}^{-3})$		1
β		1
β_{cr}		1
$\Sigma_*/(M_\odot \text{ pc}^{-2})$		50
H_*/pc		100
$\kappa_{\parallel}/(\text{cm}^2 \text{ s}^{-1})$		$3 \cdot 10^{28}$
$\dot{N}_{\text{SN}}/\text{Myr}^{-1}$		1
$E_{\text{inj,th}}/\text{erg}$	$0.9 \cdot 10^{51}$	$0.1 \cdot 10^{51}$
$E_{\text{inj,cr}}/\text{erg}$	$0.1 \cdot 10^{51}$	0

Table 1. Simulation parameters: initial values of temperature of gas T_0 , midplane gas density ρ_0 , plasma beta β , cosmic-ray beta β_{cr} , stellar surface density Σ_* (which sets gravitational acceleration), stellar scale height H_* , parallel cosmic-ray diffusion coefficient κ_{\parallel} , supernova injection rate \dot{N}_{SN} , thermal energy per injection $E_{\text{inj,th}}$, and cosmic-ray energy per injection $E_{\text{inj,cr}}$

is how supernova energy is injected. In one simulation, named CRInj, each supernova has 10% of its energy injected as cosmic-ray energy instead of thermal energy. In the second simulation, named NoCRInj, each supernova has all of its energy injected as thermal energy, with no cosmic-ray component. The important parameters for each simulation are shown in Table 1.

The simulations are on a Cartesian grid, with the \hat{x} and \hat{y} directions spanning the midplane of the slab and the \hat{z} direction extending perpendicular to the midplane. The midplane has an area $1 \text{ kpc} \times 1 \text{ kpc}$, but the simulation extends $\pm 2.4 \text{ kpc}$, above and below the midplane, for a total simulation volume of $1 \text{ kpc}^2 \times 4.8 \text{ kpc}$. Each direction has a resolution of $\Delta x = \Delta y = \Delta z = 10 \text{ pc}$, resulting in 100 resolution elements in the \hat{x} and \hat{y} directions, but 480 in the \hat{z} direction.

The simulation is initially in hydrostatic equilibrium, and the setup is identical to the one in Habegger et al. (2023). The gravitational acceleration profile is determined by a stellar mass density Σ_* with a $\text{sech}^2(z/H_*)$ vertical distribution, resulting in

$$\mathbf{g}(z) = -2\pi G \Sigma_* \hat{z} \tanh\left(\frac{z}{H_*}\right). \quad (12)$$

Taking the cosmic-ray pressure P_c and magnetic pressure $P_B = B^2/2$ to be proportional to the gas pressure P_g , and then assuming the equilibrium is isothermal with $P_g \propto \rho$, the initial condition is

$$\frac{\rho(z)}{\rho_0} = \frac{P_g(z)}{P_{g,0}} = f(z) = \text{sech}^\eta\left(\frac{z}{\eta H_*}\right), \quad (13)$$

where $\eta = H_*/H$ is the ratio of stellar scale height H_* to gas scale height

$$H = \frac{k_B T_0}{2\pi G \Sigma_* m_p} \left(1 + \frac{1}{\beta} + \frac{1}{\beta_{\text{cr}}}\right). \quad (14)$$

Using the function $f(z)$ in Equation 13, we can define the cosmic-ray pressure with a cosmic-ray beta $\beta_{\text{cr}} = P_{g,0}/P_{c,0}$ and the magnetic field with a plasma beta $\beta = 2P_{g,0}/B_0^2$:

$$P_c = \frac{P_{g,0}}{\beta_{\text{cr}}} f(z) \quad (15)$$

$$\mathbf{B} = \hat{x} \sqrt{\frac{2P_{g,0}}{\beta}} f(z). \quad (16)$$

All velocities are initially set to zero, and the \hat{z} and \hat{y} components of the magnetic field are set to 0 everywhere.

Note that the gravitational profile we chose for this equilibrium (Equation 12) is unrealistic, particularly at large $|z|$ outside of the midplane, because (1) it does not include a contribution from the dark matter halo and (2) it assumes an infinite plane stars with the vertical density profile $\rho_*(z) = \Sigma_*/(2H_*) \text{sech}^2(z/H_*)$. At large $|z|$, the dark matter halo will have more of an impact and the finite size of the galaxy will become important. Both of these effects will decrease the vertical component of gravitational acceleration.

The finite size of the galaxy results in less acceleration because there are less stars than assumed in the infinite plane approximation, producing less acceleration. The dark matter's effect is less obvious: the dark matter halo produces a radial acceleration, towards the galactic center. This additional matter does mean a larger acceleration, but it will be in the radial direction, not only in the vertical direction. This acceleration is still smaller than what we get assuming an infinite plane.

So, we are over-estimating the vertical gravitational acceleration on gas at large z . Any outflow velocities we find in Section 3 are therefore weaker than in a more realistic gravitational acceleration profile. Another consideration would be the Coriolis force, but that would again only serve to increase the velocities beyond what we find in our simulation.

2.2. Heating and Radiative Cooling

We include heating along with optically thin radiative cooling of the ISM in our simulations. We use a source term defined by the net heat-gain function (negative of the heat-loss function):

$$\mathcal{L}(n, T) = n\Gamma - n^2\Lambda(T). \quad (17)$$

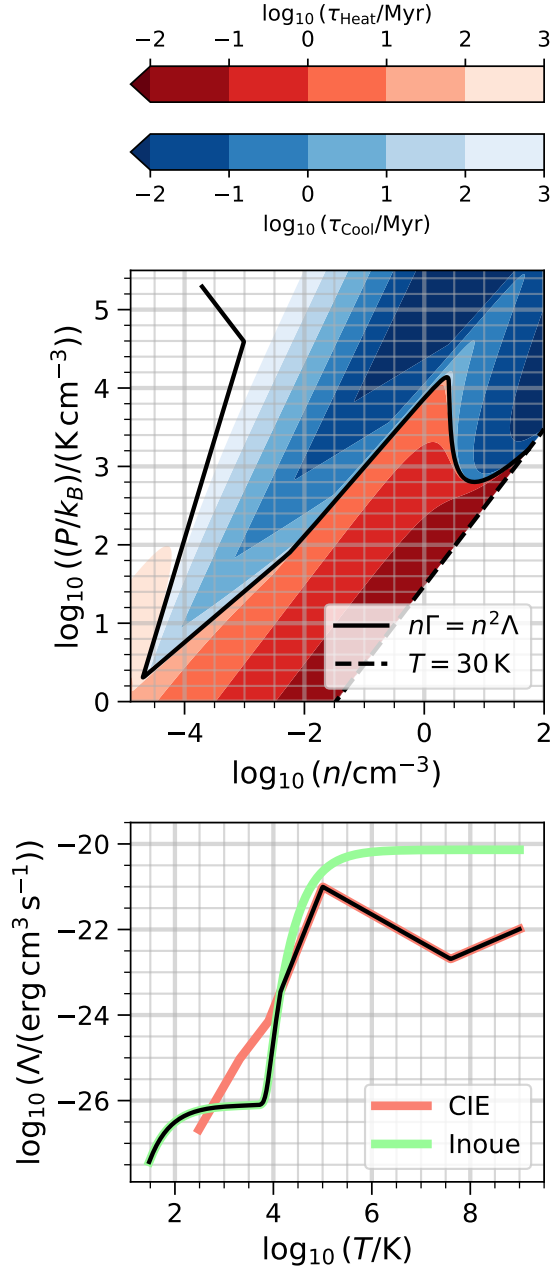


Figure 2. *Top:* Our combined radiative heating and cooling rate \mathcal{L} in Equation 17 gives equilibrium states shown as a black line in this gas pressure-gas density phase diagram. We plot our temperature floor as a dashed line in the bottom right of the plot. The contours show the net heating rate in red contours and net cooling rates in blue contours, with darker colors being faster rates. *Bottom:* We use the radiative cooling rate Λ , as a function of gas temperature T , given by the black line. This rate stitches together two functions, one from Inoue et al. (2006) (light green curve) as well as a polynomial fit to the Collisional Ionization Equilibrium (CIE) cooling rate from Rosen & Bregman (1995). We transition between these curves at their intersection of $T = 1.40413 \cdot 10^4 \text{ K}$.

We adopt the cooling function (in units of $\text{erg cm}^3 \text{ s}^{-1}$, with temperature T in units of K)

$$\Lambda(T) = \begin{cases} \Lambda_{\text{IK06}}(T) & T < 14041.3 \\ 4.624 \cdot 10^{-36} T^{2.867} & 14041.3 \leq T < 10^5 \\ 1.78 \cdot 10^{-18} T^{-0.65} & 10^5 \leq T < 4 \cdot 10^7 \\ 3.2217 \cdot 10^{-27} T^{0.5} & 4 \cdot 10^7 \leq T \end{cases} \quad (18)$$

which combines the cooling function from Rosen & Bregman (1995) along with the cooling function from Inoue et al. (2006), which has the functional form

$$\Lambda_{\text{IK06}}(T) = 7.3 \times 10^{21} \exp\left[\frac{-118400}{T + 1500}\right] + 7.9 \times 10^{27} \exp\left[\frac{-92}{T}\right]. \quad (19)$$

The cooling functions from Rosen & Bregman (1995) and Inoue et al. (2006) are plotted in the bottom graph of Figure 2. We stitch them together at $T = 1.40413 \cdot 10^4 \text{ K}$, where they intersect. The resulting curve, our cooling function, is shown as a black line in the bottom figure of Figure 2.

We use the heating rate from Inoue et al. (2006), a constant $\Gamma = 2 \cdot 10^{-26} \text{ erg s}^{-1}$ from photoelectric heating by dust grains (Inoue et al. 2006; Draine 2011). With all the parameters of Equation 17 set, we have an equilibrium curve defined by $\Gamma = n\Lambda(T)$. We show this curve in pressure-density phase space as a solid black line in the top plot of Figure 2. As mentioned in Section 2.1, we start with an isothermal atmosphere. The number density ranges from $n = 1$ to approximately $n \approx 10^{-4}$. This isothermal atmosphere quickly ($\lesssim 10 \text{ Myr}$) relaxes to the equilibrium curve in that density range before the energy injections significantly adjust the structure.

In Figure 2, we also plot contours for the net isochoric cooling and heating time:

$$\tau = \frac{k_B T}{\gamma - 1} \frac{1}{\Gamma - n\Lambda(T)}. \quad (20)$$

In Figure 2, the red areas are where $\tau > 0$ in Equation 20, giving net heating. The blue areas are where $\tau < 0$, resulting in net cooling. We plot the isochoric time because we use an operator split approach, including the heating and radiative cooling as an isochoric process. Adiabatic compression and expansion are already included in the energy evolution (see Equation 4). This treatment is common, e.g. see Townsend (2009). Unlike the exact method in Townsend (2009), we use an explicit integration for the heating and radiative cooling, with order set by the MHD time integrator. Explicit integration is reasonable for our simulations because our

cooling time is longer than the simulation’s time step ($\Delta t = \text{CFL} \times \Delta x / V_m \sim 65.2 \text{ yr}$), which is set by the modified speed of light V_m .

Examining Figure 2, we see at higher densities $n \gtrsim 10^{-2} \text{ cm}^{-3}$ the gas cools or heats on short timescales, until it again reaches the equilibrium curve where heating and cooling balance. We also plot our floor temperature of $T = 30 \text{ K}$ as a dashed line in the top plot of Figure 2. Whenever the gas reaches the temperature floor, we turn off the radiative heating and cooling terms. If the gas is compressed or expanded by gas motions and brought above the temperature floor, then the terms are again included.

An important caveat is that our resolution of 10 pc is rather large when attempting to study the thermal instability created by the cooling curve from Inoue et al. (2006). Therefore, the shapes of cold dense structures formed in our simulation are not reliable. There should be fragmentation down to smaller scales than we resolve. The resolution also limits the peak gas density in the simulations. However, we will see in Section 3 that the development of the thermal instability is resolved by multiple gas cells. Without a curve like the one from Inoue et al. (2006), we would not form cold gas through Field’s thermal instability (Field 1965) because there would not be a strong turnover in the pressure-density phase space. By using the Inoue et al. (2006) curve, the initial production of unstable gas is closer to what is expected in the Milky Way’s ISM.

Another aspect of our implementation to note is that our radiative heating mechanism of a constant Γ for all gas densities and vertical positions is unrealistic. The heating rate should fall off with vertical position z , allowing more radiative cooling to occur outside the midplane. This choice makes it harder for gas to cool at large z where gas densities are also lower (lower density reduces the cooling term more than it reduces the heating term in Equation 17). However, choosing a constant Γ makes the thermodynamic equilibrium curve (top panel of Figure 2) the same for the entire simulation volume, instead of the curve being dependent on position. This simplification makes it easier isolate the effect of the energy injections on the state of the gas.

2.3. Energy Injections

We inject energy at random locations in the midplane. We restrict the midplane to be cells with vertical coordinate between $z = \pm H_* = \pm 100 \text{ pc}$. To set the location of an injection, we select one of these cells from a random distribution proportional to the gas density in each cell, effectively following a Kennicutt-Schmidt law, $\text{SFR} \propto \rho^n$, with $n = 1$ (Kennicutt et al. 2007; Joung

et al. 2009). While there is initially no positional preference in the xy plane, the injections are more likely to occur inside dense gas at later times once density variations have developed.

The number of injections in each timestep Δt is taken from a Poisson distribution, with parameter $\lambda = \dot{N}_{\text{SN}} \Delta t$ (see Table 1). After calculating the number of injections, we generate their locations using the aforementioned method. This randomization of number of injections makes our simulations stochastic in time, despite having a fixed injection rate \dot{N}_{SN} . We keep \dot{N}_{SN} constant so we can isolate the impact of including cosmic-ray injections. For a more realistic and complete stellar feedback loop, we would need to tie the injection rate to the amount of cold gas in the simulation (assuming the amount of cold gas is a tracer of star formation rate).

Once the number of injections and their locations are determined, we fill a cube with sides of length $L = 100 \text{ pc}$ centered on the injection location with a uniformly distributed thermal energy $E_{\text{inj,th}}$ and uniformly distributed cosmic-ray energy $E_{\text{inj,cr}}$. These energy values change between the CRInj and NoCRInj simulations (see Table 1). It is important to note this limits the accuracy of thermal feedback at the end of the simulation once a significant amount of cold gas has formed. The Sedov-Taylor phase ends at smaller radii for a supernova in a higher density medium, so the evolution of the thermal energy profile is inaccurate (see numerical implementations of energy injection like Kim & Ostriker (2015) for solutions to this problem). As a result, we underestimate the total thermal feedback, in particular the conversion to momentum feedback, towards the end of the simulation.

This caveat does not apply as significantly to the cosmic-ray feedback. Since the cosmic-ray energy is predominantly diffusive in the high density regime (because of decreased Alfvén speed), the cosmic-ray energy quickly diffuses along the local magnetic field. However, our 10 pc resolution could limit the accuracy of the local magnetic field structure around energy injection sites. A more resolved magnetic field could amplify the cosmic-ray feedback on small scales. Additionally, we do not include cosmic-ray momentum boost of supernovae explosions (Diesing & Caprioli 2018), or a local decrease in the cosmic-ray diffusion coefficient in star formation regions (Semenov et al. 2021). These additional complexities in cosmic-ray transport would primarily change cosmic-ray feedback in the midplane, but would have a smaller impact on larger length scales ($L \gtrsim 1 \text{ kpc}$) and longer timescales ($t > 1 \text{ Myr}$) we consider.

2.4. A Note on Parker Instability

Our initial conditions are overall similar to setups used to examine the Parker instability (Parker 1966). We tested multiple setups in the single injection simulations and found disruption by the injection is dependent on the Parker stability criterion (Habegger et al. 2023). Our initial setup in this work (see Table 1) is linearly unstable to the Parker instability. Since we begin with an isothermal atmosphere, the linear instability criterion (only considering a plane-parallel atmosphere) is (Newcomb 1961; Zweibel 2017; Heintz & Zweibel 2018):

$$1 + \frac{1}{\beta} + \frac{1}{\beta_{\text{cr}}} > \gamma_g + \gamma_c \frac{1}{\beta_{\text{cr}}} \quad (21)$$

and plugging in the values from Table 1, we find $\gamma_c < \frac{4}{3}$. Since we include non-advective transport like streaming and diffusion, we expect to satisfy this criteria and the setup is then unstable.

We can also estimate the growth rate of the most unstable mode. Following the dispersion relations derived in Heintz & Zweibel (2018), we use the 3D Modified Parker (non-zero γ_c) with streaming transport case. For our setup, we find the most unstable Fourier mode has a wavelength along the magnetic field of $L_x \sim 0.85$ kpc, and a growth rate of $\tau \sim 33$ Myr. Additionally, all the the wavelengths above $L_x \geq 0.35$ kpc are unstable. Those large scale wavelengths are all above the size of our injections, which are a box of side length $L = 100$ pc (see Section 2.3).

3. RESULTS

We now describe the results of our two simulations, named **CRInj** and **NoCRInj**. A key similarity between the simulations is the development of two stages in time. We describe this time evolution before a detailed examination of each stage. The first stage is related to the exponential growth of the Parker instability, while the second stage is a steady state which develops after the Parker instability has disrupted the initial hydrostatic equilibrium. Finally, we compare our simulations to observational diagnostics.

3.1. Time Evolution

We run the simulations for 400 Myr. Initially, the entire setup is destabilized by many energy injections. These perturbations drive the Parker instability, producing a fountain flow which begins at approximately 100 Myr into the simulation. At 200 Myr the simulation begins to settle into a steady state structure. This steady state lasts from approximately 250 Myr until the end of the simulation at 400 Myr.

These evolutionary stages are apparent in Figure 3, which illustrates how the different components of energy

density evolve over time. The left column of Figure 3 shows the results from the **CRInj** simulation, and the right column shows the results from the **NoCRInj** simulation.

In the top row of Figure 3, we show the directional components of kinetic energy density for each simulation. During the initial destabilization, most of the motion ends up being vertical, perpendicular to the mid-plane. Before $t \sim 250$ Myr, the **CRInj** simulation produces more kinetic energy in every component direction than the **NoCRInj** simulation. Therefore, the additional cosmic-ray pressure from the injections has a significant impact on the dynamics of the gas. In the eventual steady state after $t \sim 250$ Myr the kinetic energy in each component levels off to a constant value. The kinetic energy parallel to the mean magnetic field (\hat{x} direction) ends up being the largest. The spikes are due to individual energy injections, which quickly dissipate. A key difference between the simulations in the steady state is the ordering. In the **CRInj** simulation, the vertical kinetic energy is distinctly larger than the planar motion perpendicular to the magnetic field (\hat{y} direction). However, the **NoCRInj** simulation has these energies at about the same value.

The middle row of Figure 3 shows the time evolution of the directional components of magnetic energy density. Both simulations have a similar evolution - the magnetic field starts only in the \hat{x} direction, and this energy decays because magnetic flux in the \hat{x} and \hat{y} direction can escape out of the top and bottom of the simulation box. The magnetic energy density in the vertical direction increases, exponentially, until approximately $t \sim 180$ Myr. In Section 3.2, we show this increase is tied to the Parker instability's characteristic structure. After $t \sim 180$ Myr, the magnetic energy density decays. This decay might be offset by amplification due to shearing if we had included galactic rotation in our models. Additionally, we observe numerical magnetic reconnection, which contributes to the loss of magnetic energy density.

The bottom row of Figure 3 compares the evolution of total thermal, magnetic, kinetic, and cosmic-ray energy density. The total kinetic energy density is much lower than the cosmic-ray, magnetic, and thermal energy densities. The thermal energy density has continual spikes as a result of the energy injections, but an underlying decrease as cold, dense gas forms from optically thin radiative cooling. The total magnetic energy reflects the decrease in the \hat{x} directed component and the spike in vertically directed magnetic field. Finally, the cosmic-ray energy density shows the biggest difference between the two simulations. The **CRInj** simulation shows a lin-

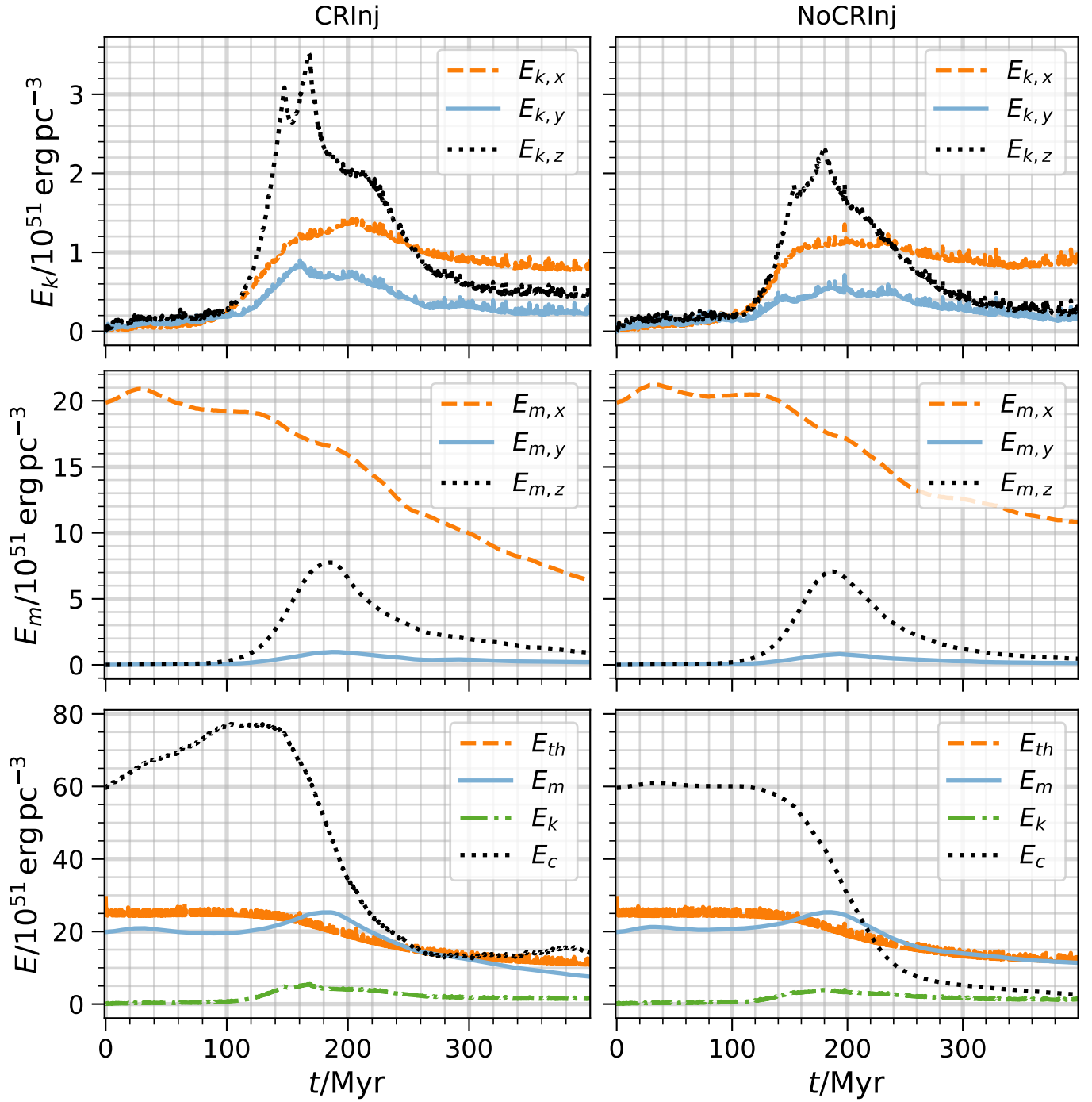


Figure 3. The time evolution of energy density averaged over the simulation volume in simulations CRInj (left column) and NoCRInj (right column). The top row shows the kinetic energy density divided into its directional components (\hat{x} , \hat{y} , \hat{z}), and the middle row shows the same for magnetic energy density. The bottom row compares thermal energy density, total magnetic energy density, total kinetic energy density, and cosmic-ray energy density.

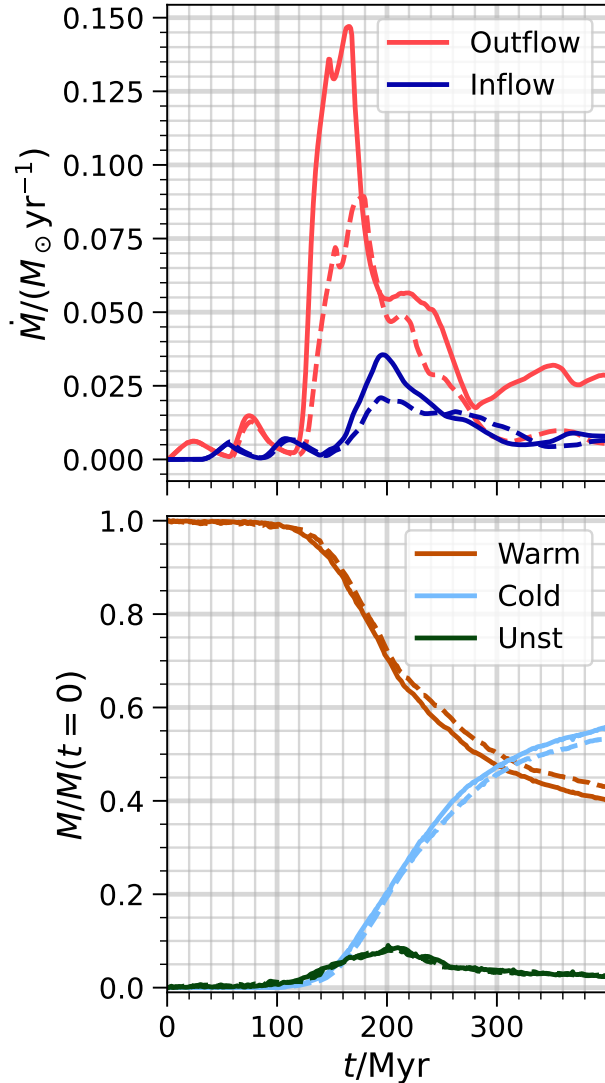


Figure 4. *Top:* Mass outflow and inflow rates for regions above and below the midplane ($|z| > 1$ kpc). Solid lines show the CRInj simulation and dashed lines show the NoCRInj simulation. *Bottom:* Mass fraction of different phases in terms of the initial mass in the simulation. After $t = 0$, the sum of these phases can be less than one because mass can flow out of the top and bottom boundaries. Again, the solid lines show the CRInj simulation and the dashed lines show the NoCRInj simulation.

ear increase early on as the cosmic-ray energy injections add to the background cosmic-ray energy density. Both simulations show a decrease in cosmic-ray energy density which is tied to the increase in vertical magnetic field. Since the cosmic rays are stuck to the local magnetic field, there needs to be magnetic flux directed out of the top and bottom of the simulation to allow the cosmic-ray energy to escape. As the vertical magnetic field energy density decreases, the cosmic-ray energy density levels off in the NoCRInj simulation. The CRInj simulation

also levels off, but increases slightly due to continuing cosmic-ray energy injections.

Moving on from energy evolution, we focus on mass evolution in the simulations. The top graph of Figure 4 shows the mass inflow and outflow rates outside of the midplane ($|z| > 1$ kpc). The solid lines show the CRInj simulation and the dashed lines show the NoCRInj simulation. The cosmic-ray injections lead to a larger peak mass outflow (and inflow) rate, and drive a larger steady outflow. In the NoCRInj simulation, the inflow and outflow nearly balance each other at late times ($t > 300$ Myr). There also appears to be a fountain flow component, where outflows are followed by inflows at a delay of about ~ 30 Myr at the start of the simulations. Finally, the two simulation curves are almost exactly the same until $t \sim 100$ Myr, which reflects that the simulations were run with the same random seed.

In the bottom of Figure 4, we show the mass fractions of different gas phases. We define warm gas as gas with temperature $4 \cdot 10^3 \text{K} \lesssim T \lesssim 10^5 \text{K}$, unstable gas as gas with temperature $100 \text{K} \lesssim T \lesssim 4 \cdot 10^3$, and cold gas is gas with temperature $T \lesssim 100 \text{K}$. In pressure-density phase space (see Figure 2) the warm gas stretches between the minimum of the equilibrium curve up to the peak above a gas density of 1cm^{-3} . The unstable gas is between that peak and the minimum just below a density of 10cm^{-3} , and the cold gas ranges from that minimum to the temperature floor of $T = 30 \text{K}$. It should be noted that the lines in this plot do not necessarily add to unity at each time. There is a small loss of mass out of the outflow boundaries which causes the total mass to decrease by a factor of $\lesssim 3\%$ over the 400 Myr of evolution.

Overall, we see that initially ($t \lesssim 120$ Myr) some thermally unstable gas is created, which eventually becomes cold gas. The lack of a significant mass fraction of unstable gas is characteristic of weak multiphase turbulence (Ho et al. 2024). That observation is consistent with our simulations - most of the kinetic energy in our simulations are vertical, and associated with the bulk outflow in the top panel of Figure 4.

After the unstable gas forms, the cold gas quickly becomes the dominant component of the overall mass fraction after $t \sim 300$ Myr for both simulations. There is a slight delay in the NoCRInj simulation, which is shown with dashed lines. The peak in unstable gas formation tracks with the inflow rate in the top plot of Figure 4. This correlation suggests a connection between the fountain flow and the formation of cold gas via thermal instability. In Section 3.2, we show this connection comes from a combination of the Parker instability and Field's thermal instability.

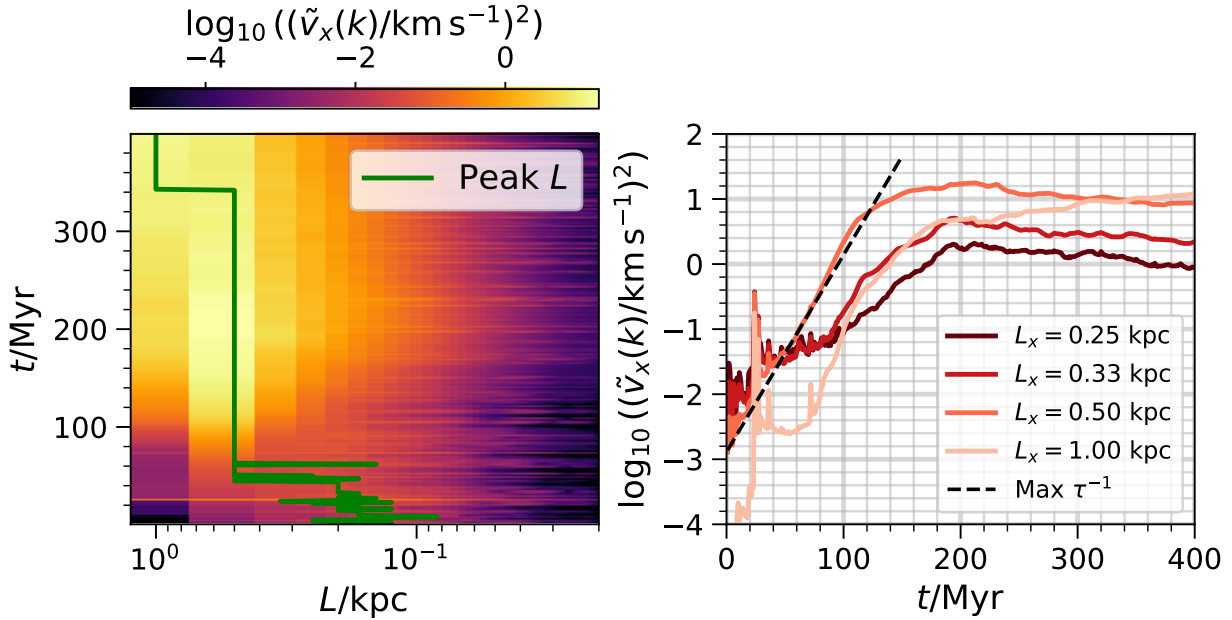


Figure 5. *Left:* Kinetic energy spectrum $\tilde{v}_x^2(k)$ (in units of $\text{km}^2 \text{s}^{-2}$) for the CRInj simulation at each 1 Myr time dump. The color map shows the amplitude of velocity fluctuations at each wavelength and the green line traces the peak wavelength of the spectrum. *Right:* Amplitude over time of the four longest wavelength Fourier modes, along with a line showing the maximum growth rate predicted by linear theory.

3.2. Parker Instability

Now we examine the initial development of the Parker instability during the beginning of the simulation, $t \lesssim 200$ Myr. First, we illustrate that the growth of the Parker instability is due to large scale velocity fluctuations which grow linearly out of the small scale energy injections we input. This behavior is characteristic of the Parker instability (for comparison, consider the small velocity perturbations used in Heintz et al. (2020)).

Figure 5 shows the evolution of the kinetic energy spectrum. We calculate the spectrum in a 1 kpc^3 volume centered on the midplane - specifically, we only include cells with $|z| \leq 0.5 \text{ kpc}$, matching the length of the x and y directions. On the left side of Figure 5, we show the time evolution of the entire kinetic energy spectrum. Most of the energy is at small scales $L \lesssim 0.3 \text{ kpc}$ for the first 50 Myr, but the gradual growth of the Parker unstable mode(s) at large scales eventually takes over. The wavelength with the most energy at each time 1 Myr is plotted as a green line. This line locks onto a large scale mode, $L_x = 0.5 \text{ kpc}$, after approximately $t = 50$ Myr. This transition to a dominant Parker instability growth is also apparent when we look at the time evolution of the four largest scale Fourier modes in the right side of Figure 5. Initially, the smallest scales have the most energy. Then, the $L_x = 0.5 \text{ kpc}$ Fourier mode surpasses the other wavelengths while its total energy grows at a rapid rate, near the maximum rate predicted by linear

theory (33 Myr, see Section 2.4). At around 150 Myr, the amplitude of that mode saturates. This saturation is significantly faster than $\sim 0.5 \text{ Gyr}$ saturation timescale which previous Parker instability simulations have found (Heintz et al. 2020; Tharakal et al. 2023). After the saturation point, the mode decays in amplitude but the largest scale mode $L_x = 1 \text{ kpc}$ increases. Eventually, the box size mode $L_x = 1 \text{ kpc}$ becomes dominant at late times ($t > 340$ Myr).

Although the saturation time is likely impacted by our limited box size along the magnetic field, the rapid outflow begins a little before the saturation (see top plot of Figure 4). This outflow means the dynamical impact of the Parker instability still happens sooner than expected.

Now, we focus on the growth and saturation of the large scale modes of the Parker instability. Figure 6 shows slices of the CRInj simulation at time $t = 165$ Myr and $y = -0.395 \text{ kpc}$. These slices illustrate saturation of the Parker instability, with plumes which erupt from the simulation's midplane, also producing valleys of cold gas. The left plot of Figure 6 shows the velocity of the gas in the simulation, whereas the right plot shows the cosmic-ray pressure. Both plots have magnetic field lines and gas density contours overlaid. The gas density contours are selected to only be around gas which is thermally unstable.

The plume is moving upward at $v_z \lesssim 100 \text{ km s}^{-1}$. The cosmic-ray pressure is higher inside of the rising

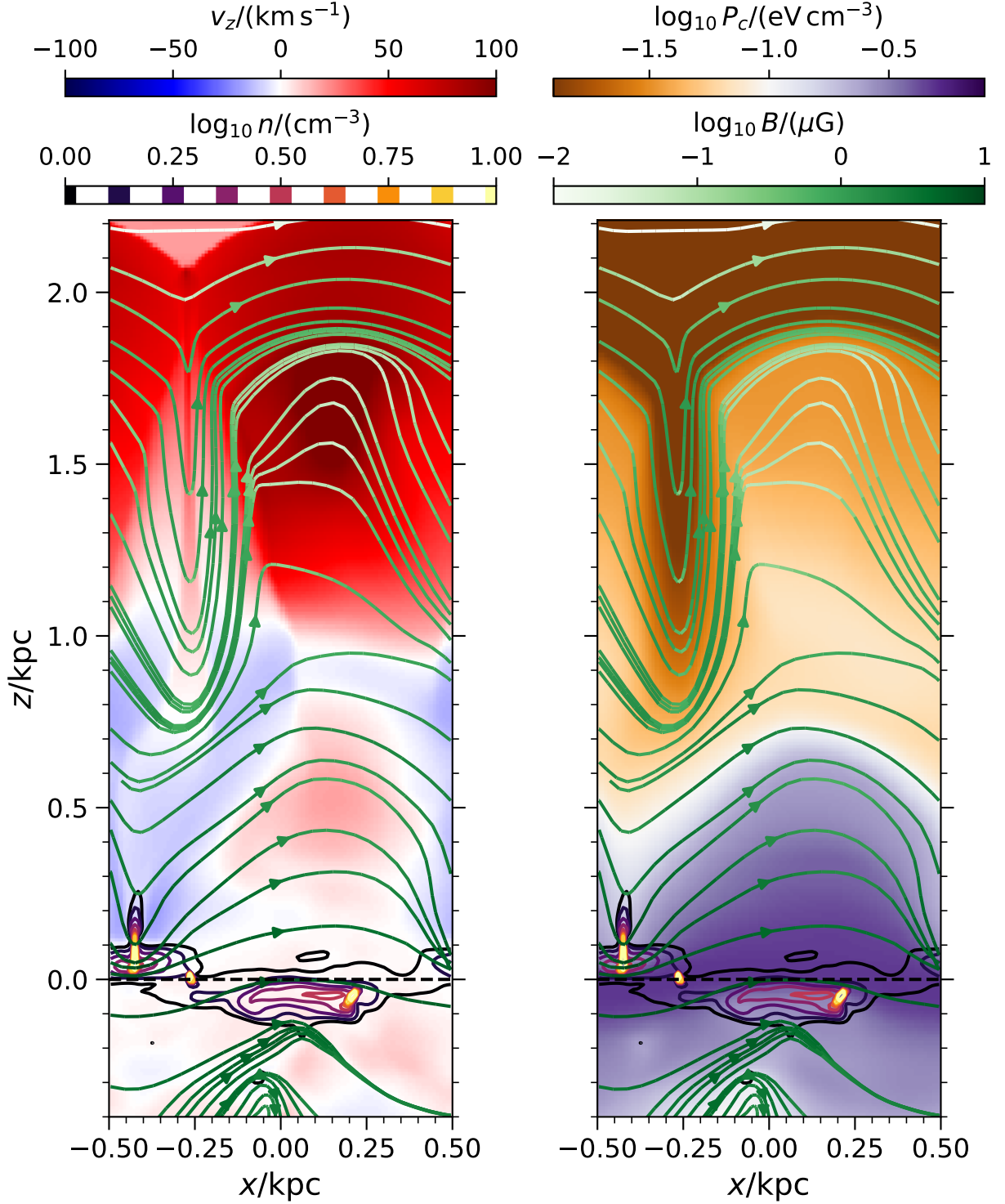


Figure 6. *Left:* Vertical velocity colormap with gas density contours and magnetic field lines overlaid. The large plume centered at $x \sim 0.1 \text{ kpc}$ is moving upward at a fast rate ($v_z \sim 50 - 100 \text{ km s}^{-1}$). *Right:* Colormap of cosmic-ray pressure with gas density contours and magnetic field lines overlaid. The density contours highlight the thermally unstable gas phase which forms below where the plume expands into itself (because of periodic boundary conditions). The plume is driven upward partly by the cosmic-ray pressure gradient, which is apparent in the colormap. Both the left and right simulation slices are taken from the CRInj simulation at $y = -395 \text{ pc}$ and at a time of $t = 165 \text{ Myr}$.

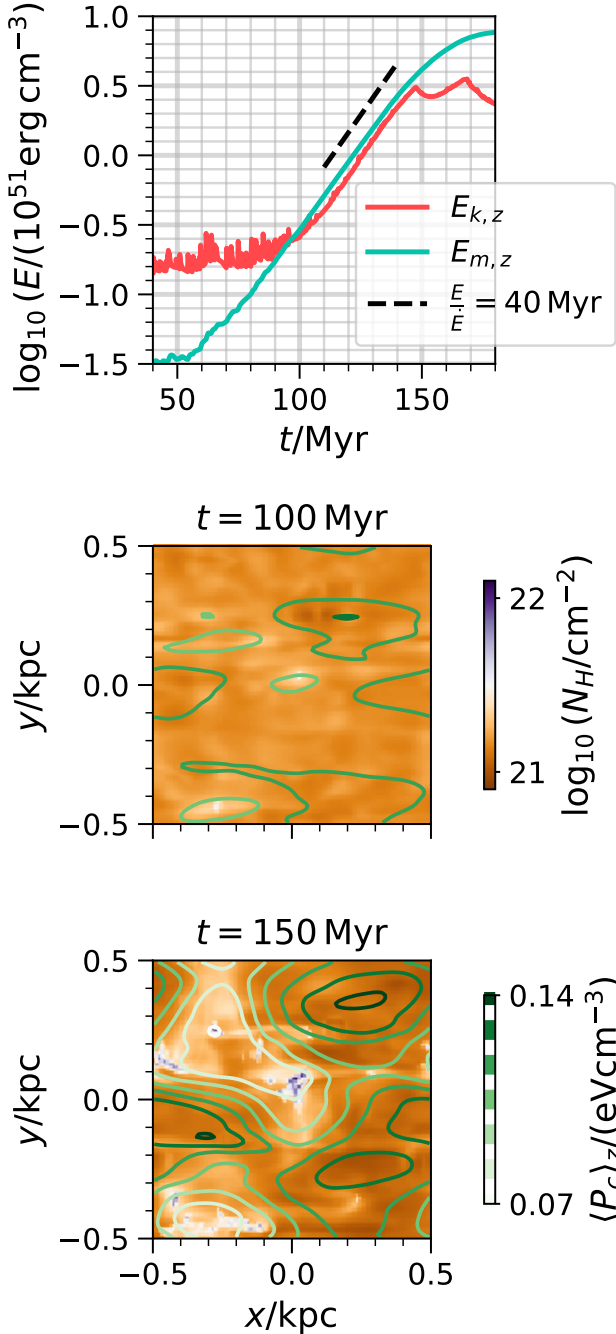


Figure 7. *Top:* Growth of vertical kinetic and magnetic energy density in the CRInj simulation is exponential with a characteristic time of $\tau \sim 40 \text{ Myr}$. *Middle:* Column density colormap and average cosmic-ray pressure contours at $t = 100 \text{ Myr}$. *Bottom:* Same as middle plot, but at $t = 150 \text{ Myr}$.

plume of gas, showing that the cosmic-ray pressure gradient is helping to drive the gas flow. The rising plume pushes gas out of the way, which then rolls off the top of the plume and falls back to the midplane along magnetic field lines. This gas compresses at $z \lesssim 0.25 \text{ kpc}$,

forming thermally unstable gas. The compressed gas also matches the picture of antisymmetric gas condensations across the midplane from each other created by the Parker instability, noted and studied in Giz & Shu (1993).

Considering both slices together, another aspect becomes clear - the regions of high cosmic-ray energy density are opposite (across $z = 0$) the regions of high gas density. cosmic-ray pressure drives the plumes, which places them spatially out of phase with the thermally unstable gas which is condensing between plumes. Therefore, the combination of the Parker instability and thermal instability can decorrelate the cosmic-ray pressure from the local gas density, an important effect in estimating the γ -ray emission of a galaxy.

Figure 7 further illustrates this decorrelation by the Parker instability. During the exponential growth of vertical kinetic and magnetic energy density (top plot), the variations in column density and average cosmic-ray pressure in the \hat{z} direction change significantly. Additionally, we find a growth rate of approximately $\tau = \dot{E}/E = 40 \text{ Myr}$ which is about the same as the $\tau \sim 33 \text{ Myr}$ growth rate predicted using a linear Parker growth rate. At $t = 100 \text{ Myr}$ (middle plot of Figure 7), the gas is fairly uniform in column density and average cosmic-ray pressure. These quantities are shown with a colormap and contour lines, respectively.

By $t = 150 \text{ Myr}$ (bottom plot of Figure 7), the Parker instability has decreased the column density of the outflowing plume regions and decreased the average cosmic-ray pressure along columns where dense gas is forming. The dense gas regions also correspond to regions where the magnetic field has become mostly vertical (see right side of Figure 6). This vertical field allows cosmic-ray energy to rapidly escape toward higher values of z since gravity does not impact cosmic-ray motion. Eventually that cosmic-ray energy leaves the simulation through the vacuum boundaries at the top and bottom of our simulation.

The Parker instability and this decorrelation may not remain in a fully turbulent galactic disk, with spiral arms driving additional gas compressions and stirring the magnetic field. But in general, the decorrelation could appear wherever the magnetic field becomes predominantly vertical outside of the midplane, giving the cosmic rays a pathway to escape.

3.3. Saturated State

The simulations develop a saturated and steady state after the Parker instability disrupts the original hydrostatic equilibrium. We focus on the time period between $t = 300 \text{ Myr}$ and $t = 400 \text{ Myr}$, even though the steady

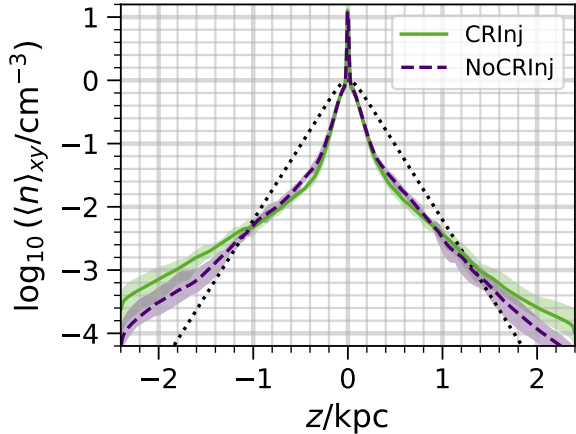


Figure 8. The average vertical density profile over the period $t = [300, 400]$ Myr. The solid green line is from the CRInj simulation and dashed purple line is from the NoCRInj simulation. We calculated the profile at every 1 Myr time dump by averaging over each xy -plane and then averaging those vertical profiles over time. The shaded regions show the full variation (min and max average density value at a given z position) for each simulation. Both simulations form a thin cold gas disk ($n > 1 \text{ cm}^{-3}$), a thin warm disk ($n < 1 \text{ cm}^{-3}$), and a thick warm gas disk ($n < 10^{-1} \text{ cm}^{-3}$).

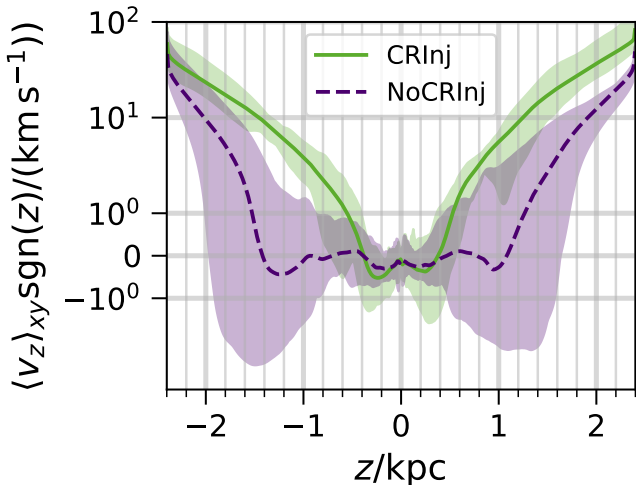


Figure 9. xy -plane averaged outflow/inflow velocities from both simulations. The averaged velocity profile over the steady state time frame ($t \in [300, 400]$ Myr) is shown for each simulation. The solid green line is from the CRInj simulation and dashed purple line is from the NoCRInj simulation. The shaded regions show the full variation of the profile over the steady state time frame. The CRInj simulation has a stronger outflow which starts from closer to the midplane.

state appears to start as early as $t = 250$ Myr in Figure 3. We start the analysis at $t = 300$ Myr to avoid the transition period from the nonlinear evolution of the Parker instability, which is more apparent in Figure 4. There, the outflow and inflow rates, as well as mass frac-

tions of each phase, only level off to consistent values by $t = 300$ Myr.

In the steady state, we focus on the vertical structure which appears in our simulation. Figure 8 shows average vertical density profiles over time. The density profiles are calculated by averaging over the xy -plane at every value of z . In Figure 8 the lines show the average profile over the time frame $t = [300, 400]$ Myr for each simulation. The shaded regions show the full variation of the profile over that time frame. The dotted line shows the initial hydrostatic equilibrium.

Figure 8 shows there is both more gas in the midplane and more gas above $|z| \sim 1$ kpc than at the start of the simulations. The spike in gas density near $z \sim 0$ is cold gas has settled after forming via thermal instability. There is a switch at large vertical positions, where gas has been pushed out by the Parker instability. This restructuring means a smaller scale height for cold, high density gas and a larger scale height for warm, low density gas. This new quasi-equilibrium appears in both simulations. So, the cosmic-ray injections have a minimal impact on the resultant density stratification, because the averaged profiles are similar in both simulations. The CRInj does end up with slightly denser gas at higher vertical positions, adjusting the scale height slightly (see Section 3.4).

Next, we can look at the flow speed in the saturated state. Figure 9 vertical profile of outflow speed. We calculate the average outflow speed at every value of z , integrating over the xy -plane. We multiply this value by the sign of the z coordinate to visualize outflow from the midplane (if the quantity is positive) and inflow to the midplane (if the quantity is negative). Figure 9 shows the outflow velocity profiles for each simulation averaged over the steady state time frame $300 \text{ Myr} < t < 400 \text{ Myr}$, and the shaded regions show the full variation in the profile over that time frame. The CRInj simulation shows a steady outflow out of the miplane (i.e. for $|z| \geq 0.5$ kpc) which could contribute to a galactic wind. This steady outflow contrasts the state in the NoCRInj simulation which shows more fluctuation between outflow and inflow in the time-averaged profile, only having a dominant outflow for $|z| \geq 1.5$ kpc. The fluctuation between outflow and inflow is also apparent in the volume integrated mass outflow and inflow rates plotted in Figure 4.

Presumably, the cosmic-ray injections are driving the outflow in the CRInj simulation, since that is the only difference between it and the NoCRInj simulation. To prove this, we calculate the average vertical pressure gradient for gas pressure, cosmic-ray pressure, and magnetic pressure (only the x and y components of the mag-

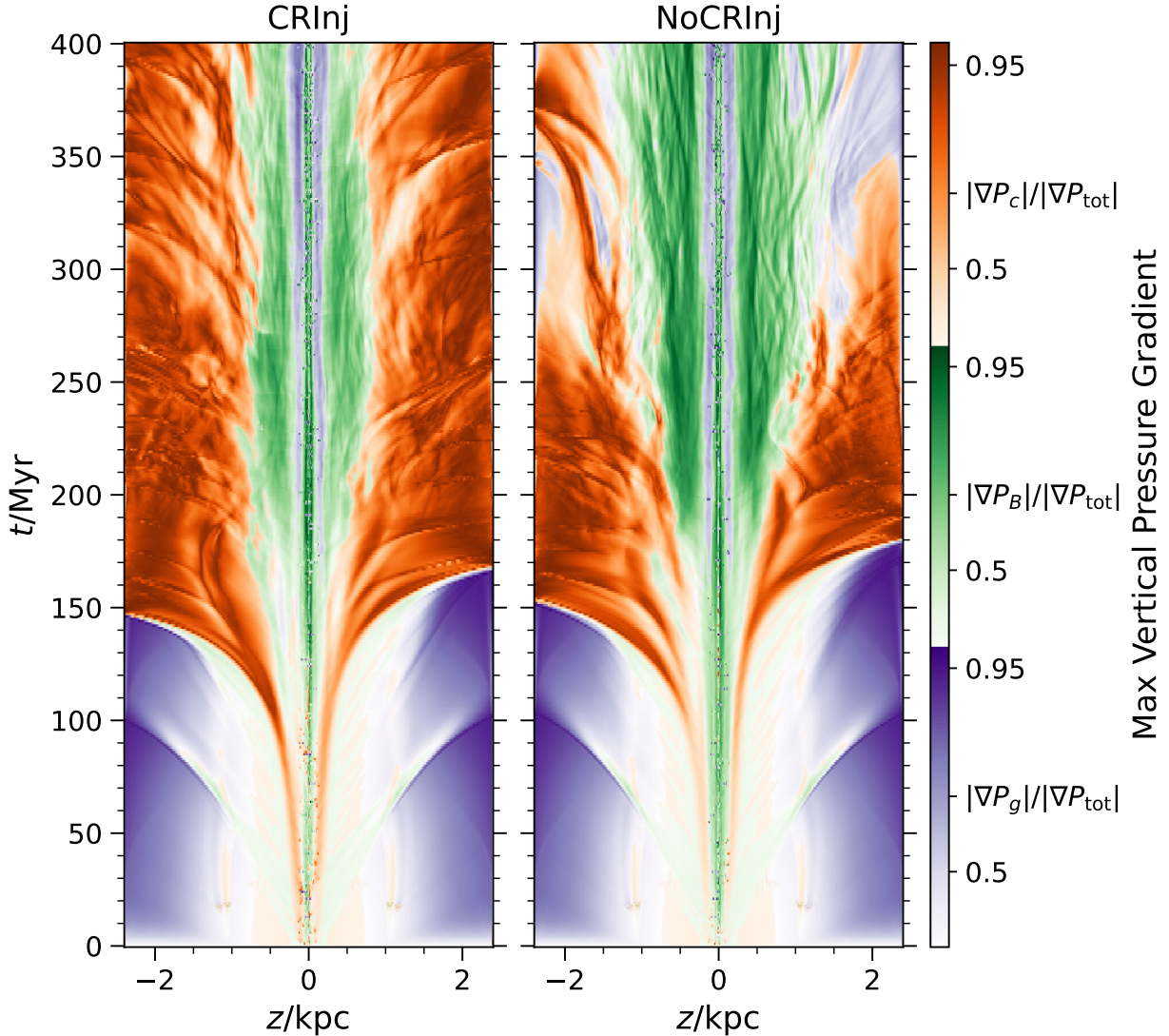


Figure 10. Spacetime diagrams of the dominant pressure gradients in the `CRInj` simulation (left column) and the `NoCRInj` simulation (right column). The lower third of the colorbar (purple) is for regions where the xy -plane averaged vertical pressure gradient is predominantly gas pressure, the middle third (green) is when the magnetic pressure gradient is dominant, and the top third (orange) is where the cosmic-ray pressure is dominant. The `CRInj` simulation has much stronger cosmic-ray pressure gradients at later times, once the magnetic field is mainly vertical.

netic field contribute) in every xy plane. We show the maximum vertical pressure gradient at each vertical position z at each time dump t in Figure 10. The primary difference between the two simulations is the large cosmic-ray pressure supported regions in the steady state period of the `CRInj` simulation. The cosmic-ray pressure is the dominant forcing term outside of the midplane ($|z| \gtrsim 1$ kpc) by a large amount, $\geq 95\%$. This cosmic-ray pressure dominance contrasts with the steady state of the `NoCRInj` simulation, which has a mix of magnetic, gas, and cosmic-ray pressure support outside of the midplane.

Both simulations show a pinched region of magnetic support in the midplane, where the gas density is high-

est, surrounded by regions of gas pressure support. This switch in pressure support within the midplane derives from the switch from cold to warm gas - the cold gas has pressure support from its magnetic field but the warm gas is supported by its own gas pressure. Outside of $|z| \sim 250$ pc, the magnetic field pressure again takes over in both simulations before falling off.

Taking a closer look at the pressure gradients, we plot the acceleration from each pressure gradient averaged over the saturated state in Figure 11. The lines show the average acceleration due to the background gravitational field (solid black line), the cosmic-ray pressure (solid orange line), the gas pressure (purple dashed line), and magnetic pressure (green dash-dotted line). The

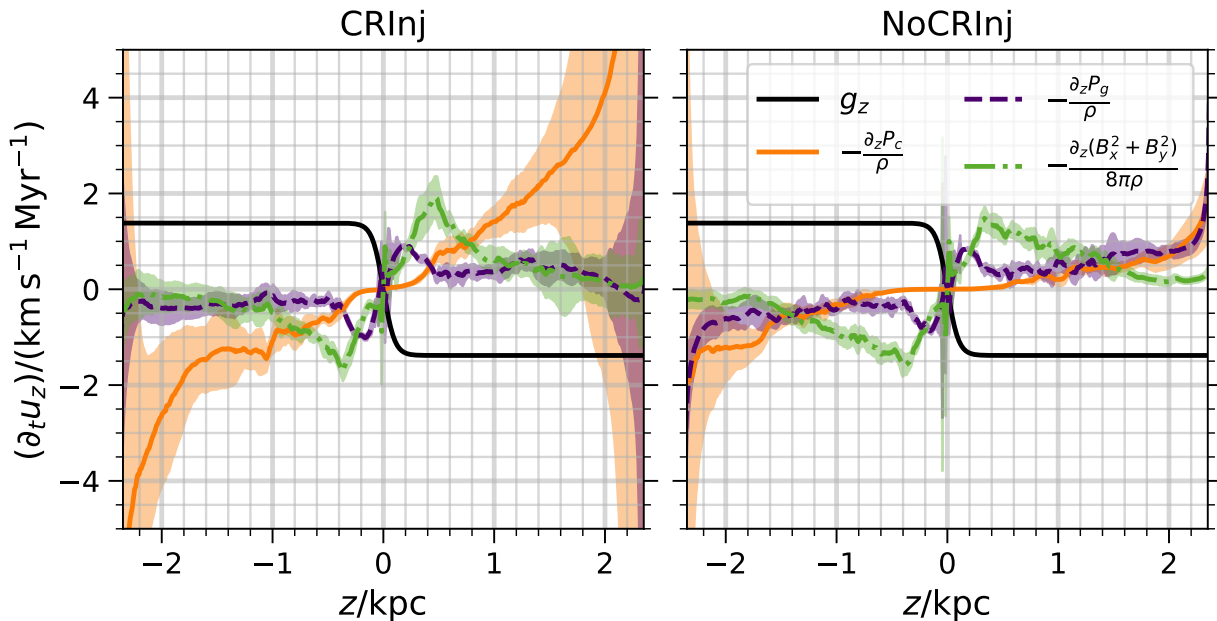


Figure 11. Vertical acceleration by various forces in the CRInj simulation (left plot) and in the NoCRInj simulation (right plot). The solid black line shows the gravitational acceleration from the background profile, the solid orange line shows the acceleration from the vertical cosmic-ray pressure gradient, the dashed purple line shows the acceleration from the gas pressure gradient, and the dash-dotted green line shows the vertical magnetic pressure gradient. Each line (except the constant gravitational acceleration) has a shaded region showing the full variation of the acceleration from the given force during the steady state time frame ($t \in [300, 400]$ Myr).

shaded regions show the full variation of the acceleration over the saturated time frame. The CRInj simulation has much more acceleration from the cosmic-ray pressure gradient term, which vanishes in the midplane. That is the only difference - the magnetic pressure and gas pressure acceleration profiles in the simulations are similar. They both peak at small z values and then fall off with height.

The net acceleration in each simulation is shown in the bottom plot of Figure 12. Both simulations have mostly outward (from the midplane) acceleration, which matches with the volume integrated inflow/outflow integration in Figure 4. These accelerations are only estimates because we do not account for the magnetic tension and the nonlinear acceleration $\mathbf{u} \cdot \nabla \mathbf{u}$ in the calculation. However, we calculated these terms and they are predominantly 0 at most times. Their averages show up as flat lines when we include them in Figure 11, so we remove them to make the figure easier to understand. However, they do have some variation ($\sim \pm 0.2 \text{ km s}^{-1} \text{ Myr}^{-1}$) which could increase or decrease the net acceleration.

The top plot of Figure 12 shows the ratio of the accelerations, illustrating that the CRInj always has more acceleration. In some places it has as much as $10\times$ the acceleration of the NoCRInj simulation. This increased acceleration further illustrates the ability of cosmic rays

to drive outflows from a galactic disk, even if they do not take over as a forcing mechanism until gas reaches the galactic halo.

The dominance of cosmic-ray pressure support in the extraplanar gas deserves more scrutiny. Why does the cosmic-ray pressure support only become significant outside the midplane? To answer this question, we have to examine cosmic-ray transport throughout our simulations.

First, we examine the magnetic field structure, which can impact the cosmic-ray transport. The rapid falling off of magnetic pressure with height in Figures 10 & 11 is partly because of a change in magnetic field orientation. The beginnings of that orientation change were apparent in the Parker instability growth pictures in Figure 6. Focusing on the averaged vertical structure, Figure 13 shows the xy -plane averaged fraction of the magnetic field in the vertical direction $b_z = |B_z|/B$. We use the absolute value because there is an equal amount of positive and negative vertical magnetic flux when integrating over each xy -plane. Above $|z| \sim 1$ kpc, the magnetic field becomes predominantly vertical in both simulations during the saturated time frame. There is more vertical magnetic field within the midplane of the CRInj simulation compared to the NoCRInj simulation (although it is still subdominant to the horizontal field). As a result, there is less magnetic pressure available to support

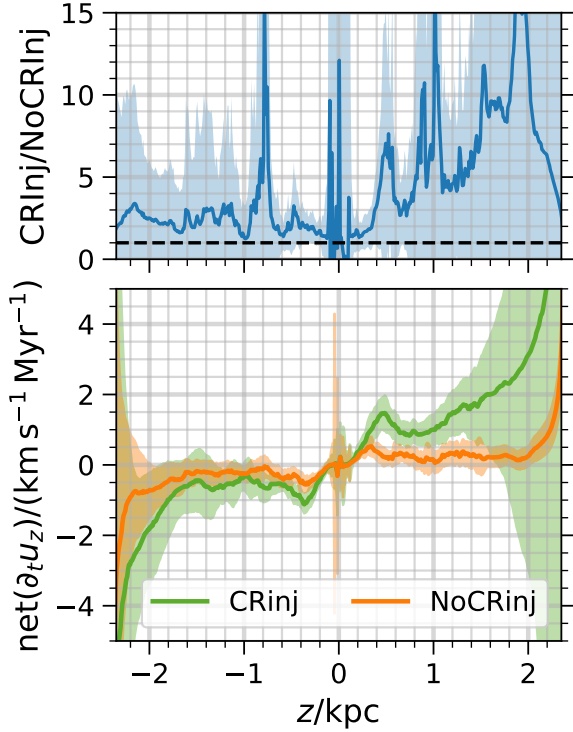


Figure 12. *Bottom:* Net acceleration in each simulation, calculated by adding up the forces in Figure 11. *Top:* Ratio of net acceleration between the CRInj simulation and the NoCRInj simulation. Except for near the midplane, the CRInj simulation always has a larger net acceleration directed away from the midplane (i.e. negative acceleration for $z < 0$ and positive acceleration for $z > 0$).

gas in the CRInj simulation. In the NoCRInj simulation, there is more horizontal field in the midplane, but the vertical field still takes over in the extraplanar gas at $|z| \gtrsim 1$ kpc.

Second, we can examine the cosmic-ray transport in the midplane compared to the transport in the extraplanar gas. In the top row of Figure 14, we show the cosmic-ray pressure-gas number density phase space. The histograms are averaged over the steady state time frame of $t \in [300, 400]$ Myr. These figures show a clear differentiation in cosmic-ray transport between the dense gas and diffuse gas. In the dense gas, cosmic rays rapidly diffuse, ending up almost uniformly distributed across orders of magnitude in gas density. Once the cosmic rays escape the dense gas, they enter the extraplanar gas which has a lower density, and high speeds, allowing advective and streaming transport to dominate. In both our simulations, the streaming transport is dominant. This streaming transport is apparent in the histograms, which do not follow the $\gamma_c = 4/3$ polytropic law ($P_c \propto n^{\gamma_c}$) for cosmic rays advected with the thermal gas. Instead, it follows a $\gamma_c = 2/3$ index, which

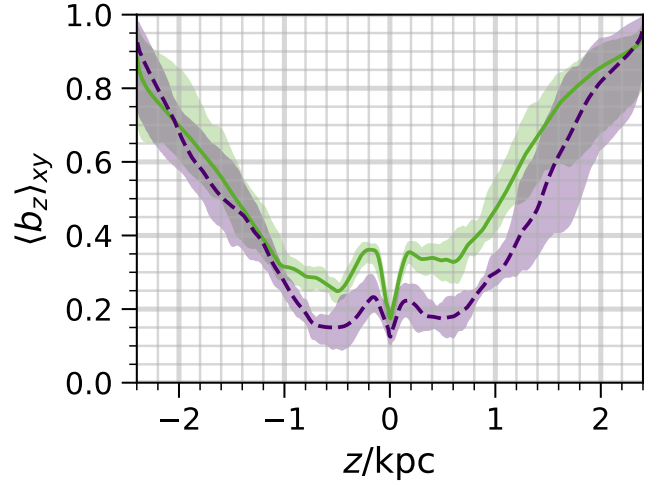


Figure 13. xy -plane averaged fraction of the magnetic field directed vertically. The lines show the average vertical magnetic field fraction for the steady state time period ($t \in [300, 400]$ Myr). The solid green line is from the CRInj simulation and dashed purple line is from the NoCRInj simulation. The shaded regions show the full variation of the profile over the steady state time frame. The CRInj simulation produces more vertical magnetic field in the midplane, resulting in a slightly lower height where the vertical field strength becomes dominant.

is expected for a steady state system with streaming transport (Wiener et al. 2019). This result is unexpected given advective and diffusive transport are also included in the simulation. Likely, since the magnetic field is predominantly vertical and aligned with the cosmic-ray pressure gradient, the streaming becomes dominant. In the CRInj simulation, there is also a spike just below $\log_{10}(n/(1\text{cm}^{-3})) = 0$. This spike comes from averaging over all the cosmic-ray injections which occur during the steady state time frame. Those injections are often in gas which is heated (moved to lower densities) by thermal feedback, and where cosmic rays propagate along the magnetic field.

Figure 14 also shows the gas pressure-gas number density phase space (middle row) and the gas temperature-gas number density phase space (bottom row). The histograms are averaged over the steady state time period. For the most part, the profiles in both simulations follow the thermal equilibrium curve of $\Gamma = n\Lambda$ shown in Figure 2 and plotted as a dashed green line in middle row plots. However, the CRInj simulation's histogram departs from this curve at low gas densities, and this low density gas is also at a higher temperature in the temperature-density phase space. This heating comes from the streaming transport of cosmic rays, which takes over in the diffuse gas. At the lower density, the net cooling time increases and is unable to offset cosmic-

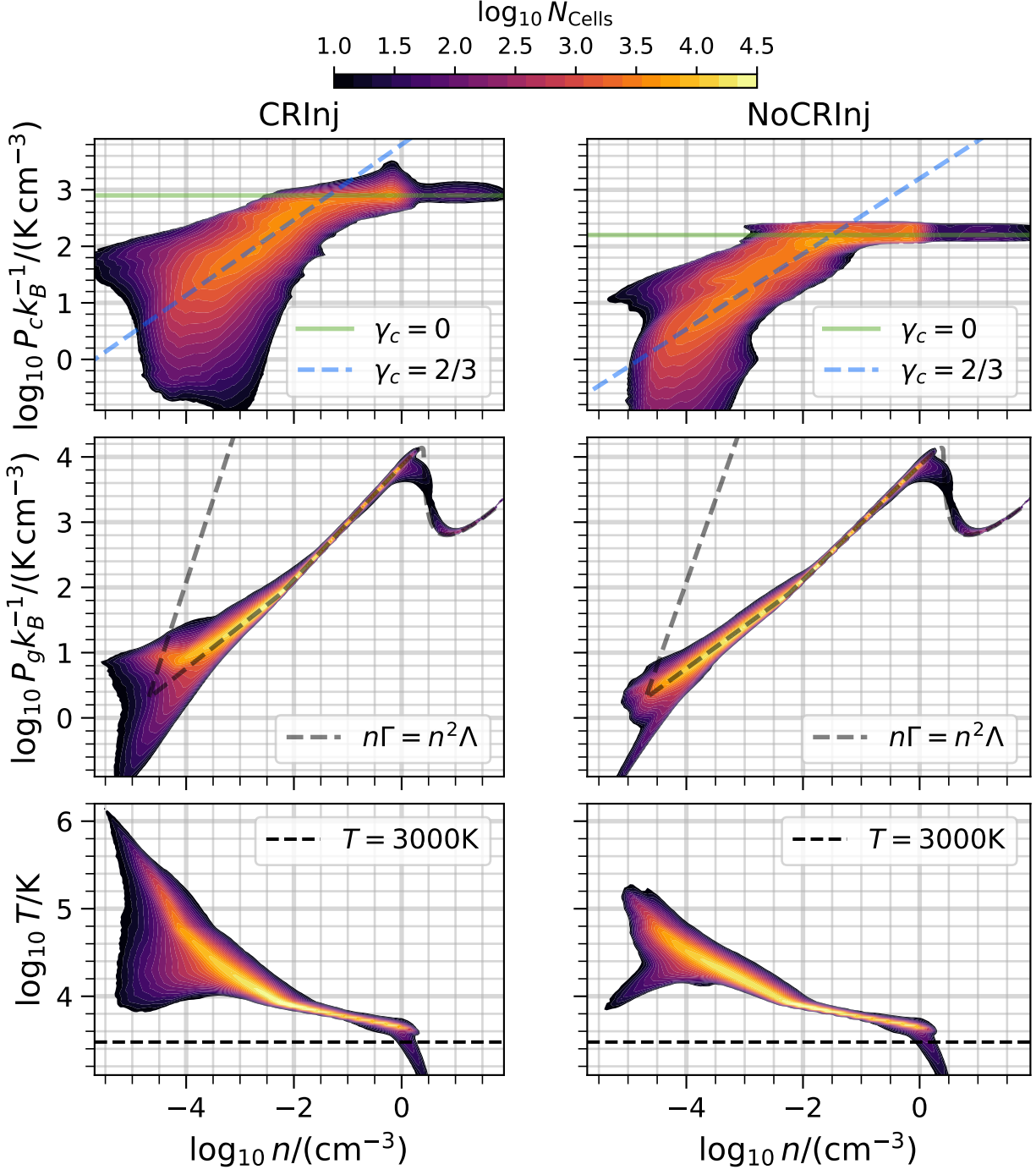


Figure 14. Average phase diagrams for the CRInj simulation (left column) and the NoCRInj simulation over the steady state time frame ($t > 300$ Myr). *Top Row:* cosmic-ray pressure-gas number density phase diagram, which show predominately diffusive transport in the high density midplane gas and predominately streaming transport in the diffuse extraplanar gas. *Middle Row:* Gas pressure-gas number density phase diagram. The histogram follows the heating cooling equilibrium curve, shown as a dashed green line (see Figure 2), except the CRInj deviates at high gas density where Alfvénic heating from the cosmic rays pushes the gas off the equilibrium curve. *Bottom Row:* Temperature-gas number density phase diagram. The CRInj ends up with higher temperature gas due to the Alfvénic heating from cosmic-ray streaming. We also plot the cut-off temperature we use to remove cold and thermally unstable gas in Section 3.4.

ray heating, leading to increased temperature. While we have not done any simulations in which streaming is present but cosmic-ray heating is removed from the energy equation, the relative paucity of low density, high temperature in the NoCRInj model demonstrates that this is an important effect.

After this examination of the steady state, a clear picture of the interplay between magnetic field orientation and cosmic-ray feedback emerges. The shift to a predominantly vertical magnetic field outside the midplane opens the door for more effective cosmic-ray feedback. While injected cosmic rays diffuse in the midplane, they stream and provide a large pressure gradient outside the midplane, producing a faster wind compared to the simulation without cosmic-ray injections. The streaming of cosmic rays also causes them to heat the thermal gas, producing hotter gas.

Before we conclude, we test our simulations against observational results. To do this, we calculate and estimate some observable properties of our simulated galactic patch.

3.4. Observational Comparison

Using our xy -plane averaging process from Section 3.3, we can fit vertical profiles and measure scale heights for the gas density, gas pressure, cosmic-ray pressure, and magnetic pressure.

Figure 15 shows the average vertical profiles and our median fit to those profiles during the saturated, steady state. The averaged data are plotted within a shaded region, which shows the total variation over the saturated time frame. We removed the cold and thermally unstable gas disk in the midplane, which is not well-resolved, by using only gas cells with a temperature $T > 3000$ K for the xy -plane averaging. We use a linear combination of the base hydrostatic equilibrium profile (see Section 2.1):

$$f(z|A, H) = A \left(\operatorname{sech} \left[\frac{z}{H_*} \right] \right)^{H_*/H}. \quad (22)$$

At each 1 Myr time dump, this gives us a pair of scale heights H_{inner} & H_{outer} and amplitudes A_{inner} & A_{outer} . The inner amplitude is always larger than the outer amplitude, and the inner scale height is always smaller than the outer scale height. We chose the above profile because of our gravitational acceleration profile. The fitted profiles are pictured for gas density and gas pressure in Figure 15, with a central peak near the midplane and large wings outside the midplane.

While the fitted scale heights we can be related to an exponential scale height for $z \geq H_*$, we caution readers against a direct comparison with observed scale heights in the Milky Way. This caution is only because of the

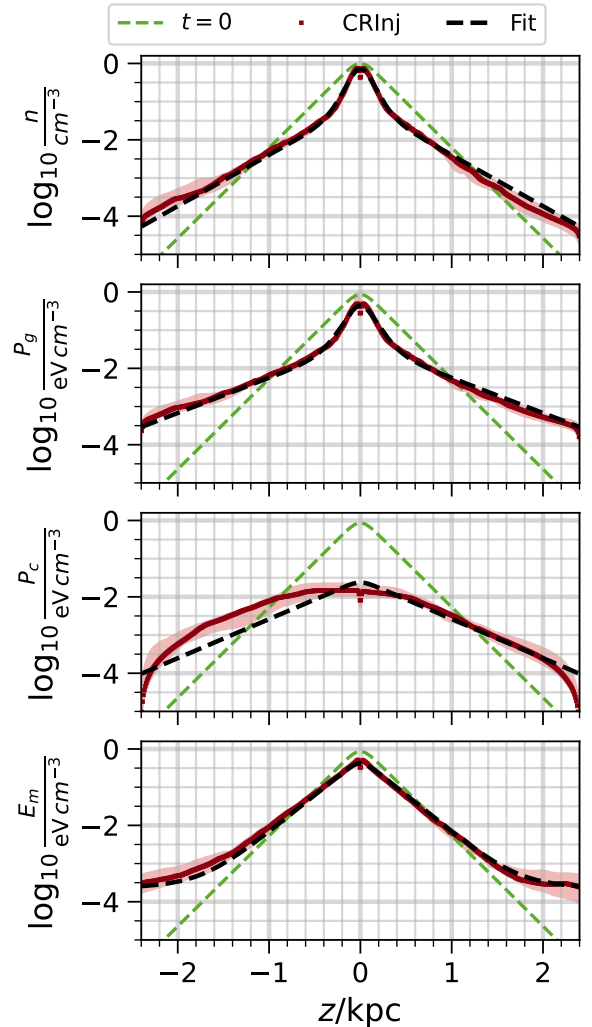


Figure 15. Average vertical profiles from the CRInj simulation, fitted with two independent scale heights. The red shaded regions show the standard deviation of the vertical profiles during the saturated time frame, and the solid red lines show the median profile. The dashed green lines show the initial hydrostatic equilibrium, and the dashed black lines show the best fit to each profile. The profiles are produced by first removing all cold gas with $T < 500$ K

less realistic gravitational acceleration profile we use (see Section 2.1). Instead, we encourage a focus on the structure which our simulations produce: a thinner, dense disk and a thicker disk inflated by non-thermal pressures. A two scale height model matches with the modern understanding of the structure of the Milky Way’s thermal gas (McClure-Griffiths et al. 2023; Rybarczyk et al. 2024).

For the non-thermal pressures, there is a different story. The cosmic-ray pressure profile in the third row of Figure 15 looks significantly different and cannot be fit by the hydrostatic equilibrium profile in Equation 22.

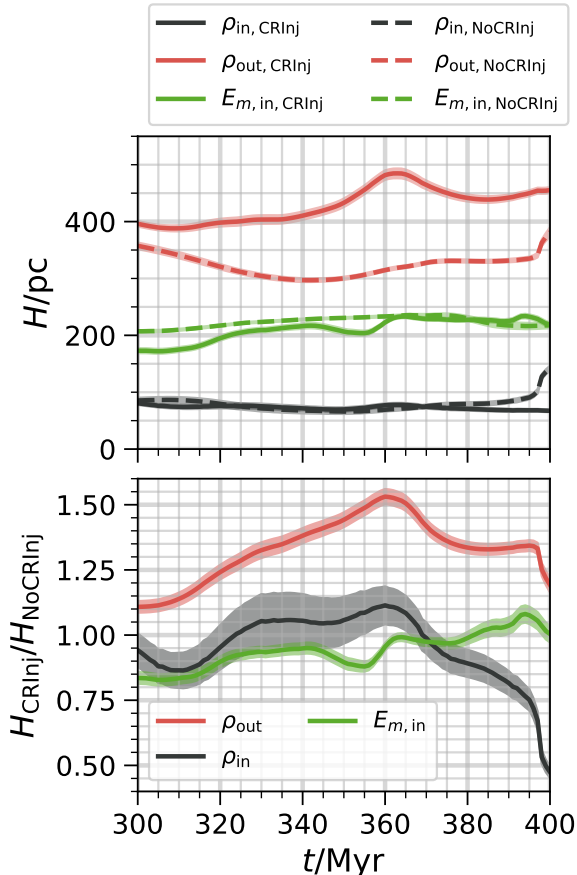


Figure 16. Ratio of gas scale heights between the CRInj simulation and the NoCRInj simulation. Black lines show the ratio of gas density scale heights, and red lines show the ratio of gas pressure scale heights. Solid lines show the outer scale height (for the lower amplitude, larger scale height component of the fits), and dashed lines show the inner scale height (for the higher amplitude, smaller scale height component of the fits).

The magnetic energy density profile at the bottom still has an inner profile and an outer profile, each following Equation 22. However, the outer profile only takes over at $z \approx \pm 1.5$ kpc instead of at $z \approx \pm 0.4$ kpc like the gas density and pressure. Figure 15 also illustrates that the gas density, magnetic field, and cosmic rays do not trace each other well.

In Figure 16, we show the time evolution of scale heights of gas density and magnetic energy density over the saturated state for both simulations. We plot these quantities because they are measurable (e.g. gas density via HI emission and absorption, and magnetic energy density through synchrotron radiation). We only plot the inner profile for the magnetic energy density because the values we measure for the outer scale height ($\gtrsim 2$ kpc) are untrustworthy. Those large values for outer scale height of the magnetic energy density are

close to the simulation’s box size and the region is very close to the vertical outflow boundaries. The only point to be taken away from the outer scale height of the magnetic energy is that it flattens out (see bottom plot of Figure 15) due to the increase in vertical magnetic field strength at large z (see Figure 13).

In the top plot of Figure 16, we see that the scale heights are relatively steady during the saturated state. The inner and outer density scale heights differ by a large factor ($\times 5$), and the magnetic energy density’s inner scale height falls in between the density scale height values. While the inner density scale height and inner magnetic energy density scale height change little when comparing the two simulations, the outer density scale height increases by over 100 pc. This inflation of the outer disk by cosmic-ray injections is more quantitatively shown in the bottom plot of Figure 16, where we take the ratio of the scale heights from each simulation. The inner gas density and magnetic energy density scale height ratio stays near 1 for most of the simulation, showing the cosmic-ray injections have a minimal impact inside the midplane region $|z| \leq 400$ pc. However, the cosmic-ray injections inflate the outer gas density scale height by between 25% and 50%.

There is another observable quantity to consider: γ -ray luminosity. This luminosity is proportional to the cosmic-ray energy density, providing a useful tool for probing the cosmic-ray content of galaxies other than the Milky Way. Cosmic rays can produce pions when they collide with non-relativistic nuclei. Some of those pions, about a third, emit γ -rays as they decay. In Figure 17, we show the evolution of the total energy lost in all hadronic interactions for our simulations. We normalize this by the cosmic-ray energy injection rate in the CRInj simulation, following the definition of the $F_{cal} = L_{\pi}/\dot{E}_{cr}$ parameter in Lacki et al. (2011). We calculate the hadronic loss rate L_{π} using the formula for the hadronic loss rate per volume Γ_h in Equation 12 of Guo & Oh (2008):

$$\begin{aligned}
 L_{\pi} &= \int_V d^3x \Gamma_h \\
 &= 8.70 \cdot 10^{44} \frac{\text{erg}}{\text{Myr}} \sum_{\text{cells}} \left(\frac{E_c}{\text{eV cm}^{-3}} \right) \left(\frac{n}{\text{cm}^{-3}} \right) \quad (23)
 \end{aligned}$$

For any subsection of the simulations, we can apply the formula in Equation 23. When calculating L_{π} , we partition the each simulation into two regions: the midplane (within a stellar scale height, $|z| \leq H_{*}$) and everything except the midplane (i.e. cells with $|z| > H_{*}$).

In the bottom plot of Figure 17, we show F_{cal} for both simulations (note that this is not the best measure for the NoCRInj simulation, which should really have

an undefined F_{cal}). Since most of the gas density is in the midplane and L_{π} is proportional to gas density (see Equation 23), most of the hadronic losses occur in the midplane. Initially, the losses are large because of the initial hydrostatic equilibrium we forced on the system (see Section 2.1). After $t \approx 250$ Myr, the hadronic losses in the NoCRInj simulation vanish much of the initial cosmic-ray background has escaped out of the top and bottom of the simulation. The emission outside the midplane in the CRInj simulation also vanishes. However, in the saturated, steady state we examined in Section 3.3, the only hadronic losses level off in the midplane of the CRInj simulation.

To get to a physically realistic and comparable F_{cal} parameter, we need to get rid of the initial background cosmic-ray pressure the simulation started with. For an approximation of this, we subtract the NoCRInj hadronic loss rate off of the CRInj hadronic loss rate. This net calorimetric fraction is plotted in the top of Figure 17 for the midplane, outside the midplane, and their combination. Initially, as cosmic-ray injections are dumped into the simulation volume, the F_{cal} increases at a constant rate. Then, at 100 Myr, when the Parker instability begins producing a strong vertical magnetic field, (see Figure 7), the net F_{cal} decreases nearly as rapidly as it rose. With the vertical magnetic field, the cosmic-ray injections are able to escape the simulation faster, producing less hadronic interactions.

As the simulation saturates, we see a steady growth of the net F_{cal} parameter. However, its growth is at a lower rate than early in the simulation, despite our cosmic-ray injection rate being constant (the injections are stochastic in time, but the average rate is constant - see Section 2.3). Since there is still some vertical magnetic fields at these times, there is more escape than at the beginning of the simulation. But that escape is still not enough to agree with observations from Lacki et al. (2011). The only time our calorimetric fraction gets close to the observational values (basically, under 0.5) is at the saturation of the Parker instability, near $t \sim 200$ Myr.

4. DISCUSSION

Returning to the original question, we find including cosmic-ray injections did make a difference. Changing the stellar feedback by putting 10% of supernova energy into cosmic rays led to a stronger outflow. It also produced a steady outflow, reaching from just 500 pc above and below the midplane out to 2.4 kpc. This steady outflow was driven by a cosmic-ray pressure gradient, which was fueled by injected cosmic rays streaming along vertical magnetic field lines.

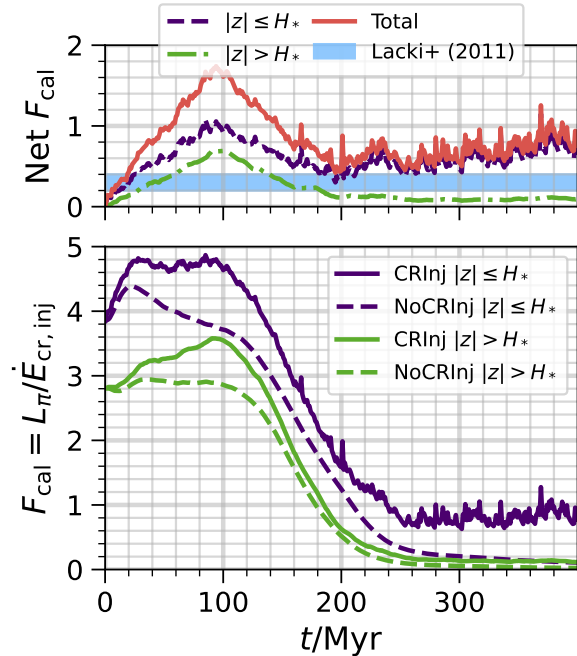


Figure 17. *Bottom:* Fraction of cosmic-ray energy injected which would be lost to hadronic interactions, following the definition of F_{cal} in Lacki et al. (2011). We plot the results for both simulations, with solid lines showing the CRInj simulation and dashed lines showing the NoCRInj simulations. We separate the emission from the midplane $|z| \leq H_*$, shown in purple, from the emission outside of the midplane, shown in green. *Top:* We calculate the Net F_{cal} by subtracting the NoCRInj simulation’s F_{cal} from the CRInj simulation’s F_{cal} . This subtraction leaves only the F_{cal} associated with our cosmic-ray injections. For comparison, the blue shaded region shows observational estimates of F_{cal} in starbursting galaxies NGC 253 and M82 (Lacki et al. 2011).

However, there were also similarities between the two simulations. The cosmic-ray injections had a minimal impact on the vertical density structure (see Figure 8). The vertical density profiles in the steady state were similar, with the only difference being an inflation of the thick disk scale height by a factor of $\gtrsim 25\%$ (see Figure 16).

Our results also suggest some solutions to other questions and problems. The CRInj simulation illustrated that the orientation of the magnetic field can have a significant impact on cosmic-ray transport. The change in transport has implications for the cosmic-ray calorimeter problem and the vertical stability of the ISM. Before we address these in Sections 4.1 & 4.2, note that these implications are not isolated to the Parker instability. The change in cosmic-ray transport we see is due to the vertical magnetic field outside of the midplane. This vertical orientation could result from the Parker instability, as it did in our simulations, or from other mechanisms.

4.1. Cosmic-Ray Calorimeter Problem

The steady state structure and change in cosmic-ray transport we see in the CRInj simulation could provide a new solution to the problem of large γ -ray luminosities in global galaxy simulations. This problem was examined in depth with the FIRE simulations in Chan et al. (2019). They found that the only way to match the observed γ -ray luminosities of lower stellar surface density galaxies was to increase the cosmic-ray diffusion coefficient. But the fundamental problem was one of calorimetry. Observational estimates have shown that smaller (lower Σ_*) galaxies are not cosmic-ray calorimeters, requiring $F_{\text{cal}} < 1$ (Lacki et al. 2011). But all of the streaming and Milky-Way diffusion coefficient simulations in Chan et al. (2019) were at or above the calorimetric limit. The “cosmic-ray calorimeter problem” is that simulated galaxies end up being cosmic-ray calorimeters. However, we calculated the F_{cal} parameter from Lacki et al. (2011) and found that our simulation got close to their observational estimates for starbursting galaxies (see top panel of Figure 17).

Our F_{cal} parameter gets close to the observed values without increased diffusion. Our cosmic rays are transported diffusively along the local magnetic field direction, like some of the simulations in Chan et al. (2019). However, combining this anisotropic transport with a higher resolution in the diffuse gas allowed the cosmic rays to escape along vertically oriented magnetic field lines. We suspect resolution is the reason this has not been noted before. Since we resolve the entire simulation at $\Delta x = 10$ pc, we resolve more of the magnetic field structure outside the midplane. For comparison with finite mass codes, a gas mass resolution of $m_g \approx 0.025 M_\odot$ would be necessary to resolve $n = 10^{-3} \text{cm}^{-3}$ gas at $\Delta x = 10$ pc. This mass resolution is much smaller than the $m_g \approx 10^3 M_\odot$ used in galaxy simulations like Chan et al. (2019).

However, the F_{cal} parameter rises again once we get numerical reconnection which reduces the amount of vertical field. The numerical magnetic reconnection occurs where the Parker instability plumes run into each other. While there is still some vertical flux which survives (see Figure 13), the reconnection decreases the total magnetic energy density (see Figure 3). It is necessary to study this process in higher resolution to determine what happens when the effects of numerical reconnection are minimized.

We suggest others also reconsider the resolution of diffuse gas outside the midplane of the galaxy when examining the cosmic-ray calorimeter problem. While the gas dynamics do not require a high resolution, it might be necessary to produce a realistic magnetic field struc-

ture. Naively, we would expect magnetic field lines could stretch from the midplane, out and up into the circumgalactic medium. Without higher resolution in the diffuse gas, these vertical field lines numerically reconnect and the region becomes disconnected from the midplane. But if the vertical field lines were still there, connecting the midplane to the diffuse gas, then they would provide an escape highway for cosmic rays. These hidden highways could be the true solution to the calorimeter problem, instead of an increased cosmic-ray diffusion coefficient.

4.2. Cosmic-Ray Transport and Stability of the Disk-Halo Interface

In our simulations, the cosmic rays are predominantly diffusive at high densities but are transported by streaming at low densities (see top row of Figure 14). This results from the density dependence of the Alfvén speed. At lower densities, the Alfvén speed gets larger, allowing the streaming transport to be larger than diffusive transport. Because of the steady stratification, this density dependence is also a vertical position dependence. In our simulations, we see cosmic rays are streaming outside of the midplane. This change in transport matches the recent results from other groups who identify the same switch in cosmic-ray transport outside the midplane (Armillotta et al. 2024; Thomas et al. 2024).

A change in cosmic-ray transport also means a change in feedback. When cosmic rays are streaming at the Alfvén speed, they heat the gas (see middle and bottom rows of Figure 14) by scattering off of Alfvén waves they generate themselves. Additionally, the streaming process is an advective process instead of a diffusive process. Instead of smoothing out cosmic-ray pressure gradients like diffusion, any steep cosmic-ray pressure gradients are advected at the Alfvén speed. So the switch to streaming means larger cosmic-ray pressure gradients, creating a larger force on the thermal gas, which can drive outflows (see Figure 10). These impacts of streaming have been discussed extensively in other works (e.g. Tsung et al. 2023).

The P_c - n diagrams in the top row of Figure 14 point to a new idea regarding cosmic-ray feedback at the disk-halo interface. When cosmic-ray transport changes, it also changes the effective polytropic index of cosmic rays. A change in polytropic index changes the stability of the system (note the appearance of γ_c in Equation 21). Our simulations show an increase in polytropic index with height. The effective polytropic index γ_c shows up on the right hand side of Equation 21, meaning an increase has a stabilizing effect. So, the change in cosmic-ray transport with z could naturally cause a fountain

flow: gas parcels moving upward because they are unstable before eventually reaching a position where their compressibility increases and they become stable to perturbations.

We developed this interpretation after reading Hosking et al. (2024), which illustrated how a plasma’s compressibility can impact the structure of metastable, stratified MHD atmospheres. A detailed analysis on the stability of a CR+MHD atmosphere is out of the scope of this paper. Instead, we just share the idea here and will examine it in detail in a future work (Habegger, Hosking & Zweibel, in prep.).

5. CONCLUSION

The simulations we have run, CRInj and NoCRInj, have illustrated the importance of cosmic-ray injections in driving outflows and structuring the ISM. Here, we list some key results from this study of cosmic-ray feedback:

1. The Parker instability drives overturning of gas which turns our initial hydrostatic equilibrium into a more realistic two-scale-height vertical gas density structure. This overturning and saturation happens on a shorter timescale than previously predicted: $\sim 150\text{Myr}$ instead of $\sim 500\text{Myr}$ (Heintz et al. 2020).
2. This overturning of gas combined with thermal instability drives the production of thermally unstable gas above the midplane, which then sinks to $z \sim 0$ while cooling. This process occurs between outflowing plumes driven, in part, by cosmic-ray pressure gradients. Our simulations show this process decorrelates cosmic-ray pressure and gas density.
3. Our simulations produce a steady state after the saturation of the Parker instability, with horizontal magnetic field in the midplane and vertical magnetic field outside the midplane. This magnetic field structure allows for more efficient cosmic-ray escape alongside significant cosmic-ray feedback and a decrease in the calorimetric fraction F_{cal} .
4. While the thin gas disk in the steady state is supported by gas pressure and some magnetic pressure, the thick gas disk is supported by non-thermal pressures. The cosmic-ray injections change the outer scale height, inflating the thick disk by a factor of up to 50%.

With only two simulations, we cannot be certain of the importance of cosmic-ray injections in all galaxies.

In particular, our work does not complete the full stellar feedback loop to show how cosmic-ray injections impact the star formation rate. To complete that loop, the injection rate would at least need to be determined by star formation rates (e.g. like in the galaxy scale simulations of Chan et al. 2019). Because we can not complete the loop, the physical process we highlight of vertical magnetic field lines being cosmic ray escape highways is just a physical explanation of decreased γ -ray luminosity. The overall effect on star formation rate of magnetic field lines connecting the disk and halo is still unclear. More simulations might illustrate the impact on star formation rate is also the same as in the increased diffusion coefficient case in Chan et al. (2019).

However, we suspect the true picture of cosmic ray feedback on star formation rates will require the increased magnetic field resolution. For example, reconsider Figure 6. In cases where the Parker instability is a dominant dynamical process, the decorrelation of cosmic rays and gas density could significantly impact star formation rates. That decorrelation was caused by field lines being vertical and not undergoing numerical reconnection. As a result, cosmic rays were able to escape the midplane before they could interact with the cold gas.

In the future, we plan to close the feedback loop while exploring the parameter space of these simulations, adjusting initial conditions and quantities listed in Table 1. Additionally, we plan to examine the steady state with a more realistic setup. In addition to tying cold gas formation and injection rate together, we could include other physical processes. Including the effects of galactic rotation (Coriolis force and shearing) would increase the fidelity the magnetic field evolution. A more realistic gravitational field would allow us to determine whether the outflows are just fountain flows or actual winds which escape the galaxy. Additionally, a more accurate heating and cooling function would produce a more realistic multiphase ISM in the simulation.

However, including all these effects will not likely change the fundamental conclusions from this paper. Our goal was to identify how cosmic rays can impact the structure and dynamics of a galactic patch. To do that, we isolated and focused on a few fundamental physical processes. Namely, a resolved magnetic field combined with cosmic-ray injections could help keep a galaxy under the calorimetric limit. The geometry of the Parker instability naturally decorrelated the cosmic rays and dense gas by generating a vertical field alongside cold gas formation. Cosmic rays will also still be efficient at driving an outflow outside of the galactic disk, where their diffusion is no longer dominant because the gas velocities and Alfvén speed increase.

1 The authors would like to thank Sophie Aerdker,
 2 Ryan Farber, Ka Wai Ho, David Hosking, Francisco
 3 Ley, Nickolas Pingel, Mohan Richter-Addo, Mateusz
 4 Ruzskowski, Aaron Tran, Bindesh Tripathi, and Ka
 5 Ho Yuen for their insight and helpful conversations
 6 which improved this work. The authors greatly appre-
 7 ciate funding from funding from NASA FINESST grant
 8 No. 80NSSC22K1749 and NSF grant AST-2007323
 9 which supported this work. Resources supporting this
 10 work were provided by the NASA High-End Computing
 11 (HEC) Program through the NASA Advanced Super-
 12 computing (NAS) Division at Ames Research Center.

Software: Athena++ (Stone et al. 2020; Jiang & Oh 2018), Matplotlib (Hunter 2007), NumPy (van der Walt et al. 2011; Harris et al. 2020), AstroPy (Astropy Collaboration et al. 2013, 2018), Wolfram Mathematica (Wolfram Research Inc. 2023)

REFERENCES

- Armillotta, L., Ostriker, E. C., Kim, C.-G., & Jiang, Y.-F. 2024, ApJ, 964, 99, doi: [10.3847/1538-4357/ad1e5c](https://doi.org/10.3847/1538-4357/ad1e5c)
- Astropy Collaboration, Robitaille, T. P., Tollerud, E. J., et al. 2013, A&A, 558, A33, doi: [10.1051/0004-6361/201322068](https://doi.org/10.1051/0004-6361/201322068)
- Astropy Collaboration, Price-Whelan, A. M., Sipócz, B. M., et al. 2018, AJ, 156, 123, doi: [10.3847/1538-3881/aabc4f](https://doi.org/10.3847/1538-3881/aabc4f)
- Baade, W., & Zwicky, F. 1934, Physical Review, 46, 76, doi: [10.1103/PhysRev.46.76.2](https://doi.org/10.1103/PhysRev.46.76.2)
- Blandford, R. D., & Ostriker, J. P. 1978, ApJL, 221, L29, doi: [10.1086/182658](https://doi.org/10.1086/182658)
- Breitschwerdt, D., McKenzie, J. F., & Voelk, H. J. 1991, A&A, 245, 79
- Bustard, C., & Zweibel, E. G. 2021, ApJ, 913, 106, doi: [10.3847/1538-4357/abf64c](https://doi.org/10.3847/1538-4357/abf64c)
- Caprioli, D., & Spitkovsky, A. 2014, ApJ, 783, 91, doi: [10.1088/0004-637X/783/2/91](https://doi.org/10.1088/0004-637X/783/2/91)
- Chan, T. K., Kereš, D., Gurvich, A. B., et al. 2022, MNRAS, 517, 597, doi: [10.1093/mnras/stac2236](https://doi.org/10.1093/mnras/stac2236)
- Chan, T. K., Kereš, D., Hopkins, P. F., et al. 2019, MNRAS, 488, 3716, doi: [10.1093/mnras/stz1895](https://doi.org/10.1093/mnras/stz1895)
- Desiati, P., & Zweibel, E. G. 2014, ApJ, 791, 51, doi: [10.1088/0004-637X/791/1/51](https://doi.org/10.1088/0004-637X/791/1/51)
- Diesing, R., & Caprioli, D. 2018, PhRvL, 121, 091101, doi: [10.1103/PhysRevLett.121.091101](https://doi.org/10.1103/PhysRevLett.121.091101)
- Draine, B. T. 2011, Physics of the Interstellar and Intergalactic Medium
- Evoli, C., Aloisio, R., & Blasi, P. 2019, PhRvD, 99, 103023, doi: [10.1103/PhysRevD.99.103023](https://doi.org/10.1103/PhysRevD.99.103023)
- Evoli, C., Morlino, G., Blasi, P., & Aloisio, R. 2020, PhRvD, 101, 023013, doi: [10.1103/PhysRevD.101.023013](https://doi.org/10.1103/PhysRevD.101.023013)
- Ferrière, K. M. 2001, Reviews of Modern Physics, 73, 1031, doi: [10.1103/RevModPhys.73.1031](https://doi.org/10.1103/RevModPhys.73.1031)
- Field, G. B. 1965, ApJ, 142, 531, doi: [10.1086/148317](https://doi.org/10.1086/148317)
- Giz, A. T., & Shu, F. H. 1993, ApJ, 404, 185, doi: [10.1086/172267](https://doi.org/10.1086/172267)
- Guo, F., & Oh, S. P. 2008, MNRAS, 384, 251, doi: [10.1111/j.1365-2966.2007.12692.x](https://doi.org/10.1111/j.1365-2966.2007.12692.x)
- Habegger, R., Ho, K. W., Yuen, K. H., & Zweibel, E. G. 2024, ApJ, 974, 17, doi: [10.3847/1538-4357/ad67da](https://doi.org/10.3847/1538-4357/ad67da)
- Habegger, R., Zweibel, E. G., & Wong, S. 2023, ApJ, 951, 99, doi: [10.3847/1538-4357/accf8e](https://doi.org/10.3847/1538-4357/accf8e)
- Harris, C. R., Millman, K. J., van der Walt, S. J., et al. 2020, Nature, 585, 357, doi: [10.1038/s41586-020-2649-2](https://doi.org/10.1038/s41586-020-2649-2)
- Heintz, E., Bustard, C., & Zweibel, E. G. 2020, ApJ, 891, 157, doi: [10.3847/1538-4357/ab7453](https://doi.org/10.3847/1538-4357/ab7453)
- Heintz, E., & Zweibel, E. G. 2018, ApJ, 860, 97, doi: [10.3847/1538-4357/aac208](https://doi.org/10.3847/1538-4357/aac208)
- Ho, K. W., Yuen, K. H., & Lazarian, A. 2024, arXiv e-prints, arXiv:2407.14199, doi: [10.48550/arXiv.2407.14199](https://doi.org/10.48550/arXiv.2407.14199)
- Hosking, D. N., Wasserman, D., & Cowley, S. C. 2024, arXiv e-prints, arXiv:2401.01336, doi: [10.48550/arXiv.2401.01336](https://doi.org/10.48550/arXiv.2401.01336)

- Hunter, J. D. 2007, *Computing in Science and Engineering*, 9, 90, doi: [10.1109/MCSE.2007.55](https://doi.org/10.1109/MCSE.2007.55)
- Inoue, T., Inutsuka, S.-i., & Koyama, H. 2006, *ApJ*, 652, 1331, doi: [10.1086/508334](https://doi.org/10.1086/508334)
- Jiang, Y.-F., & Oh, S. P. 2018, *ApJ*, 854, 5, doi: [10.3847/1538-4357/aaa6ce](https://doi.org/10.3847/1538-4357/aaa6ce)
- Jones, F. C., Lukasiak, A., Ptuskin, V., & Webber, W. 2001, *ApJ*, 547, 264, doi: [10.1086/318358](https://doi.org/10.1086/318358)
- Joung, M. R., Mac Low, M.-M., & Bryan, G. L. 2009, *ApJ*, 704, 137, doi: [10.1088/0004-637X/704/1/137](https://doi.org/10.1088/0004-637X/704/1/137)
- Kennicutt, Robert C., J., Calzetti, D., Walter, F., et al. 2007, *ApJ*, 671, 333, doi: [10.1086/522300](https://doi.org/10.1086/522300)
- Kim, C.-G., & Ostriker, E. C. 2015, *ApJ*, 802, 99, doi: [10.1088/0004-637X/802/2/99](https://doi.org/10.1088/0004-637X/802/2/99)
- Lacki, B. C., Thompson, T. A., Quataert, E., Loeb, A., & Waxman, E. 2011, *ApJ*, 734, 107, doi: [10.1088/0004-637X/734/2/107](https://doi.org/10.1088/0004-637X/734/2/107)
- McClure-Griffiths, N. M., Stanimirović, S., & Rybarczyk, D. R. 2023, *ARA&A*, 61, 19, doi: [10.1146/annurev-astro-052920-104851](https://doi.org/10.1146/annurev-astro-052920-104851)
- McKenzie, J. F., & Voelk, H. J. 1982, *A&A*, 116, 191
- Newcomb, W. A. 1961, *Physics of Fluids*, 4, 391, doi: [10.1063/1.1706342](https://doi.org/10.1063/1.1706342)
- Owen, E. R., Wu, K., Inoue, Y., Yang, H. Y. K., & Mitchell, A. M. W. 2023, *Galaxies*, 11, 86, doi: [10.3390/galaxies11040086](https://doi.org/10.3390/galaxies11040086)
- Parker, E. N. 1966, *ApJ*, 145, 811, doi: [10.1086/148828](https://doi.org/10.1086/148828)
- Rosen, A., & Bregman, J. N. 1995, *ApJ*, 440, 634, doi: [10.1086/175303](https://doi.org/10.1086/175303)
- Ruszkowski, M., & Pfrommer, C. 2023, *A&A Rv*, 31, 4, doi: [10.1007/s00159-023-00149-2](https://doi.org/10.1007/s00159-023-00149-2)
- Rybarczyk, D. R., Wenger, T. V., & Stanimirović, S. 2024, *ApJ*, 975, 167, doi: [10.3847/1538-4357/ad79f7](https://doi.org/10.3847/1538-4357/ad79f7)
- Semenov, V. A., Kravtsov, A. V., & Caprioli, D. 2021, *ApJ*, 910, 126, doi: [10.3847/1538-4357/abe2a6](https://doi.org/10.3847/1538-4357/abe2a6)
- Stone, J. M., Tomida, K., White, C. J., & Felker, K. G. 2020, *The Astrophysical Journal Supplement Series*, 249, 4, doi: [10.3847/1538-4365/ab929b](https://doi.org/10.3847/1538-4365/ab929b)
- Tharakkal, D., Shukurov, A., Gent, F. A., et al. 2023, *MNRAS*, 525, 5597, doi: [10.1093/mnras/stad2610](https://doi.org/10.1093/mnras/stad2610)
- Thomas, T., Pfrommer, C., & Pakmor, R. 2024, arXiv e-prints, arXiv:2405.13121, doi: [10.48550/arXiv.2405.13121](https://doi.org/10.48550/arXiv.2405.13121)
- Townsend, R. H. D. 2009, *ApJS*, 181, 391, doi: [10.1088/0067-0049/181/2/391](https://doi.org/10.1088/0067-0049/181/2/391)
- Tsung, T. H. N., Oh, S. P., & Bustard, C. 2023, *MNRAS*, 526, 3301, doi: [10.1093/mnras/stad2720](https://doi.org/10.1093/mnras/stad2720)
- Tsung, T. H. N., Oh, S. P., & Jiang, Y.-F. 2022, *MNRAS*, 513, 4464, doi: [10.1093/mnras/stac1123](https://doi.org/10.1093/mnras/stac1123)
- van der Walt, S., Colbert, S. C., & Varoquaux, G. 2011, *Computing in Science and Engineering*, 13, 22, doi: [10.1109/MCSE.2011.37](https://doi.org/10.1109/MCSE.2011.37)
- Wiener, J., Zweibel, E. G., & Ruszkowski, M. 2019, *MNRAS*, 489, 205, doi: [10.1093/mnras/stz2007](https://doi.org/10.1093/mnras/stz2007)
- Wolfram Research Inc. 2023, *Mathematica*, Version 13.3
- Zweibel, E. G. 2017, *Physics of Plasmas*, 24, 055402, doi: [10.1063/1.4984017](https://doi.org/10.1063/1.4984017)